The Astrophysical Journal, 958:60 (22pp), 2023 November 20 https://doi.org/10.3847/1538-4357/ad003a
© 2023. The Author(s). Published by the American Astronomical Society.
OPEN ACCESS

Early Planet Formation in Embedded Disks (eDisk). VIII. A Small Protostellar Disk around the Extremely Low Mass and Young Class 0 Protostar IRAS 15398–3359

Travis J. Thieme[1,2,3], Shih-Ping Lai[1,2,3,4], Nagayoshi Ohashi[4], John J. Tobin[5], Jes K. Jørgensen[6], Jinshi Sai (Insa Choi)[4], Yusuke Aso[7], Jonathan P. Williams[8], Yoshihide Yamato[9], Yuri Aikawa[9], Itziar de Gregorio-Monsalvo[10], Ilseung Han[7,11], Woojin Kwon[12,13], Chang Won Lee[7,11], Jeong-Eun Lee[14], Zhi-Yun Li[15], Zhe-Yu Daniel Lin[15], Leslie W. Looney[16], Suchitra Narayanan[8], Nguyen Thi Phuong[7,17], Adele L. Plunkett[5], Alejandro Santamaría-Miranda[10], Rajeeb Sharma[6], Shigehisa Takakuwa[4,18], and Hsi-Wei Yen[4]
[1] Institute of Astronomy, National Tsing Hua University, No. 101, Section 2, Kuang-Fu Rd., Hsinchu 30013, Taiwan
[2] Center for Informatics and Computation in Astronomy, National Tsing Hua University, No. 101, Section 2, Kuang-Fu Rd., Hsinchu 30013, Taiwan
[3] Department of Physics, National Tsing Hua University, No. 101, Section 2, Kuang-Fu Rd., Hsinchu 30013, Taiwan
[4] Academia Sinica Institute of Astronomy and Astrophysics, 11F of Astro-Math Bldg., No. 1, Section 4, Roosevelt Rd., Taipei 10617, Taiwan
[5] National Radio Astronomy Observatory, 520 Edgemont Rd., Charlottesville, VA 22903, USA
[6] Niels Bohr Institute, University of Copenhagen, Øster Voldgade 5-7, DK-1350, Copenhagen, Denmark
[7] Korea Astronomy and Space Science Institute, 776 Daedeok-daero, Yuseong-gu, Daejeon 34055, Republic of Korea
[8] Institute for Astronomy, University of Hawai'i at Mānoa, 2680 Woodlawn Dr., Honolulu, HI 96822, USA
[9] Department of Astronomy, Graduate School of Science, The University of Tokyo, 7-3-1 Hongo, Bunkyo-ku, Tokyo 113-0033, Japan
[10] European Southern Observatory, Alonso de Cordova 3107, Casilla 19, Vitacura, Santiago, Chile
[11] Division of Astronomy and Space Science, University of Science and Technology, 217 Gajeong-ro, Yuseong-gu, Daejeon 34113, Republic of Korea
[12] Department of Earth Science Education, Seoul National University, 1 Gwanak-ro, Gwanak-gu, Seoul 08826, Republic of Korea
[13] SNU Astronomy Research Center, Seoul National University, 1 Gwanak-ro, Gwanak-gu, Seoul 08826, Republic of Korea
[14] Department of Physics and Astronomy, Seoul National University, 1 Gwanak-ro, Gwanak-gu, Seoul 08826, Republic of Korea
[15] University of Virginia, 530 McCormick Rd., Charlottesville, VA 22904, USA
[16] Department of Astronomy, University of Illinois, 1002 West Green St., Urbana, IL 61801, USA
[17] Department of Astrophysics, Vietnam National Space Center, Vietnam Academy of Science and Techonology, 18 Hoang Quoc Viet, Cau Giay, Hanoi, Vietnam
[18] Department of Physics and Astronomy, Graduate School of Science and Engineering, Kagoshima University, 1-21-35 Korimoto, Kagoshima, Kagoshima 890-0065, Japan
Received 2023 April 27; revised 2023 October 3; accepted 2023 October 3; published 2023 November 13

Abstract

Protostellar disks are an ubiquitous part of the star formation process and the future sites of planet formation. As part of the Early Planet Formation in Embedded Disks large program, we present high angular resolution dust continuum (∼40 mas) and molecular line (∼150 mas) observations of the Class 0 protostar IRAS 15398–3359. The dust continuum is small, compact, and centrally peaked, while more extended dust structures are found in the outflow directions. We perform a 2D Gaussian fitting and find the deconvolved size and 2σ radius of the dust disk to be 4.5×2.8 au and 3.8 au, respectively. We estimate the gas+dust disk mass assuming optically thin continuum emission to be $0.6M_J$–$1.8M_J$, indicating a very low mass disk. The CO isotopologues trace components of the outflows and inner envelope, while SO traces a compact, rotating disk-like component. Using several rotation curve fittings on the position–velocity diagram of the SO emission, the lower limits of the protostellar mass and gas disk radius are $0.022\,M_\odot$ and 31.2 au, respectively, from our Modified 2 single power-law fitting. A conservative upper limit of the protostellar mass is inferred to be $0.1\,M_\odot$. The protostellar mass accretion rate and the specific angular momentum at the protostellar disk edge are found to be in the range of $(1.3\text{–}6.1) \times 10^{-6}\,M_\odot\,\mathrm{yr}^{-1}$ and $(1.2\text{–}3.8) \times 10^{-4}\,\mathrm{km\,s^{-1}\,pc}$, respectively, with an age estimated between 0.4×10^4 yr and 7.5×10^4 yr. At this young age with no clear substructures in the disk, planet formation would likely not yet have started. This study highlights the importance of high-resolution observations and systematic fitting procedures when deriving dynamical properties of deeply embedded Class 0 protostars.

Unified Astronomy Thesaurus concepts: Circumstellar disks (235); Observational astronomy (1145); Protostars (1302); Radio astronomy (1338); Radio interferometry (1346); Star formation (1569); Stellar accretion disks (1579); Young stellar objects (1834)

1. Introduction

Protostellar disks are essential for transferring mass to the central protostar and forming future planetary systems. Kinematic observations of these disks provide a way to determine dynamical protostellar masses, which is a key aspect in understanding the evolution of young protostars. T Tauri and pre-main-sequence (Class II/III) protostars harbor clear, rotationally supported disks, allowing for derivations of their dynamical masses (e.g., Simon et al. 2000; Guilloteau et al. 2014; Sheehan et al. 2019; Boyden & Eisner 2020). For deeply embedded (Class 0/I) protostars, dynamical mass derivations are complicated by the kinematics of the larger-scale envelopes (e.g., Yen et al. 2015a). Nonetheless, interferometric observations have provided a possibility to detect rotationally supported Keplerian disks at these early stages (e.g., Tobin et al. 2012; Murillo et al. 2013; Ohashi et al. 2014; Yen et al. 2014, 2017a, 2017b, 2019; Aso et al. 2015; Maret et al. 2020;

Original content from this work may be used under the terms of the Creative Commons Attribution 4.0 licence. Any further distribution of this work must maintain attribution to the author(s) and the title of the work, journal citation and DOI.

Sai et al. 2020). Thus, executing high angular resolution observations can shed light on the formation and early evolution of protostellar disks.

Rotationally supported disks in the Class 0 stage are typically studied via position–velocity (PV) diagrams of optically thin molecular line emission along the inferred disk axis. The PV structure is then compared to and/or fit with a Keplerian rotation power-law profile (e.g., Ohashi et al. 2014; Aso et al. 2017; Yen et al. 2017a; Maret et al. 2020). A rotational profile proportional to $v \sim r^{-1/2}$ corresponds to a Keplerian rotating disk, whereas a rotational profile proportional to $v \sim r^{-1}$ indicates infalling material with conserved angular momentum. The methodology for fitting PV diagrams has been developed over the years and tested against simulations (Harsono et al. 2015; Aso & Machida 2020). These results confirm that fitting peak positions/velocities in the PV diagram can accurately recover crucial properties, in particular the dynamical protostellar mass.

Additionally, deeply embedded disks likely also represent the places where planet formation is initiated. Gaps and rings are clearly revealed by observations of later-stage disks in both dust continuum (e.g., ALMA Partnership et al. 2015; Andrews et al. 2018) and molecular line emission (e.g., Öberg et al. 2021). These substructures are thought to be where planet formation is currently ongoing. Recent observations of protostars that are still in the embedded stages have also revealed the same types of substructures (Segura-Cox et al. 2020; Sheehan et al. 2020), indicating that planet formation may begin earlier than previously thought. These results are substantiated by studies indicating early grain growth (Harsono et al. 2018) and that the dust reservoir in these early disks is enough to produce observed exoplanetary systems (Tychoniec et al. 2020). However, these ring and gap structures can also form as a result of gravitational instabilities, tidal processes, dust processes, and more (see Bae et al. 2022, for a full review).

In this paper, we present new, high angular resolution Atacama Large Millimeter/submillimeter Array (ALMA) observations of the young protostar IRAS 15398–3359 (hereafter IRAS15398) as part of the Early Planet Formation in Embedded Disk (eDisk) large program. IRAS15398 is located in the B228 region of the Lupus I molecular cloud. Several recent studies derive the distance to Lupus I using Gaia DR2 data (Dzib et al. 2018; Galli et al. 2020; Zucker et al. 2020; Santamaría-Miranda et al. 2021). We adopt a distance of 155.5 pc by taking the average distances of sources and positions closest to the R.A. and decl. of IRAS15398 from these previous studies. Based on recent spectral energy distribution fittings, it is classified as a Class 0 protostar with $T_{\rm bol} = 50$ K and $L_{\rm bol} = 1.4\,L_\odot$ (Ohashi et al. 2023). This is consistent with classifications in previous studies, which have also considered other evolutionary indicators, such as the chemistry and outflow properties (Bjerkeli et al. 2016b; Vazzano et al. 2021).

Kinematic studies of IRAS15398 analyze the infalling−rotating envelope around an inferred Keplerian disk (Oya et al. 2014; Yen et al. 2017a; Okoda et al. 2018). Initial studies were not able to resolve a Keplerian disk and instead infer an upper limit on the protostellar mass using simple envelope models (Oya et al. 2014; Yen et al. 2017a). Oya et al. (2014) use an infalling−rotating envelope model to constrain the central protostellar mass to $M_\star \leqslant 0.09\,M_\odot$ using observations of several H_2CO transitions with an angular resolution of $0\farcs60 \times 0\farcs44$. Additionally, Yen et al. (2017a) use $C^{18}O$ ($J = 2 \rightarrow 1$) emission at an angular resolution of $0\farcs53 \times 0\farcs49$ to fit a rotational power-law profile to points from their PV diagram. Although they found a power-law index of -1.0 ± 0.06, indicating that the emission traces the infalling protostellar envelope, the disk was not resolved in their observations. An upper limit on the protostellar mass was found to be $\sim$0.01 $M_\odot$, along with an upper-limit disk radius of 20^{+50}_{-20} au and an inclination angle of 70°. However, if the infall is slower than the freefall assumption used in their analysis, the protostellar mass would be a lower limit. Higher-resolution ($0\farcs2$) observations were later performed, and a rotationally supported disk was inferred by comparing the PV emission structure of SO ($J_N = 7_6 \rightarrow 6_5$) to a Keplerian rotation power-law profile (Okoda et al. 2018). A profile assuming a dynamical protostellar mass of $0.007^{+0.004}_{-0.003}\,M_\odot$ and an inclination angle of 70° matched well by eye with the overall PV diagram emission. These studies indicate a relatively small, difficult-to-detect Keplerian disk around an extremely low-mass protostar. Systematic fitting procedures of the protostellar disk emission in the PV diagram at a higher resolution have yet to be implemented for this source to derive its properties.

A number of different studies on IRAS15398 provide clues to the interesting nature of the disk and protostar. The core-scale magnetic field strength has been derived to be 78 μG using polarization observations from the SOFIA telescope (Redaelli et al. 2019). Using the ratio of the turbulent and uniform magnetic field components, they conclude that the core is strongly magnetized. In this case, magnetic braking could be efficient at removing the angular momentum of infalling material and thus hindering the growth of a large disk (e.g., Mellon & Li 2008; Hennebelle & Ciardi 2009). The current primary outflow is estimated to have a dynamical timescale of $\lesssim$1000 yr (Bjerkeli et al. 2016b) and also is episodic in nature (Vazzano et al. 2021). This is complemented by evidence of a past episodic accretion event in the past 100–1000 yr (Jørgensen et al. 2013; Bjerkeli et al. 2016a). These previous studies further highlight the importance of our new higher angular resolution observations to understand the nature of the IRAS15398 system.

This paper is organized as follows. Section 2 describes the eDisk observations of IRAS15398 and a summary of the data reduction process. Section 3 presents the dust continuum and molecular line maps. We analyze the nature of the dust continuum and the dynamical properties of the protostellar disk in Section 4. In Section 5 we discuss the implications of our results and compare them to the previous studies of IRAS15398. Finally, we conclude our results in Section 6.

2. Observations and Data Reduction

Observations of IRAS15398 were carried out with ALMA as part of the eDisk large program (project ID: 2019.1.00261.L; PI: N. Ohashi) with additional short-baseline (SB) data taken as part of a complementary Director Discretionary Time (DDT) program (project ID: 2019.A.00034.S). The general characteristics of the observations are summarized in Table 1. An extensive description of the procedure for the eDisk data reduction, including links to the scripts, is provided in Ohashi et al. (2023). In this section, we summarize the key aspects of the data reduction and imaging for IRAS15398.

Table 1
Summary of eDisk Observations of IRAS 15398–3359

Parameters	Short Baseline	Long Baseline
Project ID	2019.A.00034.S	2019.1.00261.L
Observation dates	2021 May 6	2021 Aug 9, 2021 Aug 13–14, 2021 Oct 20
Array configuration	C43-5	C43-8
Number of antennas	45	39, 42, 43
Min–max baseline (m)	15–2517	70–8282, 70–8282, 46–8983
Phase center (ICRS)	$15^{\rm h}43^{\rm m}02^{\rm s}.24$, $-34^\circ09'06''.8$	
	Calibrators	
Bandpass	J1337−1257	J1337−1257, J1517−2422, J1427−4206
Flux	J1337−1257	J1337−1257, J1517−2422, J1427−4206
Phase	J1610−3958	J1534−3526
Pointing	J1337−1257, J1610−3958	J1337−1257, J1457−3539, J1517−2422, J1427−4206

Note. See Ohashi et al. (2023) for a detailed summary of the eDisk program, observations, and data reduction procedure.

Long-baseline (LB) observations were taken in three execution blocks on 2021 August 9 with 39 antennas, 2021 August 13–14 with 42 antennas, and 2021 October 20 with 43 antennas. Additional SB observations were taken on 2021 May 6 with 45 antennas. The data were reduced using the Common Astronomy Software Applications (CASA) package v6.2.1 (McMullin et al. 2007; CASA Team et al. 2022). Standardized eDisk reduction scripts were used for self-calibrating and imaging the SB+LB data and the SB-only data.[19] In both cases, the continuum data are self-calibrated first, followed by the molecular line data since the line self-calibration uses the self-calibration solutions from the continuum. In the case of SB-only data, five iterations of phase-only self-calibration were performed. For the combined SB+LB data, six iterations of phase-only self-calibration were performed on the SB-only visibilities, followed by four iterations of phase-only self-calibration on the combined SB+LB visibilities.

Continuum images were then produced using the CASA *tclean* task with Briggs weighting. Robust values of −2.0, −1.0, −0.5, 0.0, 0.5, 1.0, and 2.0 were used to find the image with the best balance between angular resolution and noise. Additional images with UV tapers of 3000, 2000, and 1000 kλ are also automatically produced by the script for robust values of 1.0 and 2.0. The molecular line visibilities were also aligned, scaled by flux between observations, and continuum-subtracted using the line-free channels. The self-calibration solutions from the continuum visibilities were then applied to the spectral lines and cleaned using the CASA *tclean* task with Briggs weighting and a robust value of 1.5 to obtain better signal-to-noise ratio (S/N). A summary of the representative maps that will be analyzed in this paper is listed in Table 2.

3. Results

3.1. Dust Continuum

The high angular resolution (SB+LB) 1.3 mm dust continuum maps for two robust values of +0.5 and −0.5 are shown in Figure 1. A gallery of the SB+LB continuum maps for each robust value produced by the imaging script is shown in Appendix A. The robust = +0.5 map shows extended dust emission out to a few 100 au and has a peak intensity ($I_\nu^{\rm peak}$) and brightness temperature ($T_b^{\rm peak}$) of 7.10 mJy beam^{-1} and 28.6 K, respectively. This extended emission is also seen in previous studies of this source (Oya et al. 2014; Yen et al. 2017a; Okoda et al. 2018), though it is more resolved out in our image owing to the higher angular resolution of ∼80 mas (12.4 au at 155.5 pc). The extended emission follows the overall direction of the outflow, which is indicated by the red and blue arrows in Figure 1 (left panel). The robust = −0.5 map shows a single, compact dust structure with an $I_\nu^{\rm peak}$ and $T_b^{\rm peak}$ of 5.95 mJy beam^{-1} and 93.4 K, respectively. The angular resolution of ∼40 mas (6.2 au at 155.5 pc) gives us a resolved image with respect to the beam. This resolution is ∼10 times better resolution than the previous Band 6 observations reported in Yen et al. (2017a) and ∼4 times better than the most recent Band 6 observations reported by Okoda et al. (2021, 2023). There are four, low-S/N structures at 3σ–5σ extending out ∼2 au from the central continuum emission. These structures are contiguous with the larger-scale dust emission seen in the robust = +0.5 map. In the gallery of continuum images (Figure A1), we see that as we decrease the robust value in our image cleaning, these structures, along with the large-scale emission, disappear from the image. This indicates that the structures are related to the larger-scale dust emission and just being resolved out as we increase the image spatial resolution.

We measured the geometric parameters and the integrated flux density of the robust = −0.5 dust continuum map by performing a 2D Gaussian fit in the image plane using the CASA *imfit* task. The results are shown in Figure 2 and Table 3. The residual image in Figure 2 shows that the central emission is well represented by a 2D Gaussian, and there are no clear leftover substructures within the disk. We also checked this by making intensity cuts and radial profiles, but we failed to see any sign of substructure in the disk. There are four leftover extended structures in the residual image corresponding to the extended continuum emission in the observation map. The coordinates at the peak intensity are α(ICRS) = $15^{\rm h}43^{\rm m}02^{\rm s}.232$, δ(ICRS) = $-34^\circ09'06''.96$. This position is adopted as the protostellar position of IRAS15398 for the figures and analysis in this paper. The deconvolved size ($\theta_{\rm maj} \times \theta_{\rm min}$) was found to be 29 × 18 mas (4.5 × 2.8 au at a distance of 155.5 pc), with the position angle (north to east) of the major axis being 117°.1. By assuming a geometrically thin disk, the inclination angle can roughly be estimated by

$$i = \cos^{-1}(\theta_{\rm min}/\theta_{\rm maj}), \quad (1)$$

which gives an angle of ∼50°.7. The peak intensity and integrated flux density measured by the fitting are 5.86 mJy beam^{-1} and 7.89 mJy, respectively.

The (gas+dust) disk mass can be estimated under the assumptions of entirely thermal and optically thin dust emission via

$$M_{\rm disk} = \frac{D^2 S_\nu}{\kappa_\nu B_\nu(T_{\rm dust})}, \quad (2)$$

where D is the distance to the source, S_ν is the integrated flux density, κ_ν is the dust opacity adjusted for the gas-to-dust ratio,

[19] https://github.com/jjtobin/edisk

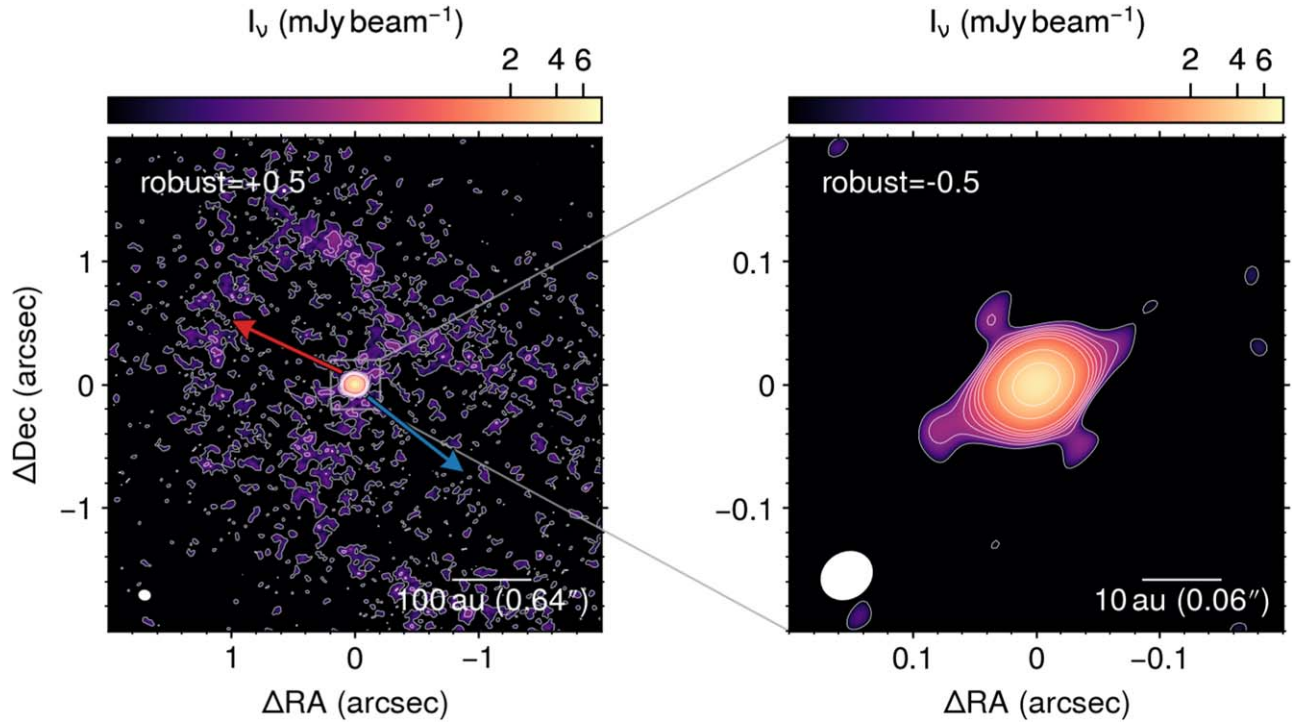

Figure 1. Representative 1.3 mm dust continuum maps of IRAS15398 with asinh ($a = 0.001$) scaling. Left: the robust = 0.5 map showing an overall view of the extended dust emission. The blue and red arrows represent the overall blue- and redshifted outflow directions found by Vazzano et al. (2021), respectively. Right: the robust = −0.5 map showing a zoomed-in view of the central compact structure. The contours in both maps are shown in steps (3, 5, 7, 9, 12, 15, 20, 50, 100)$\sigma_{\rm rms}$, where $\sigma_{\rm rms}$ is the rms noise of each map.

Table 2
Summary of SB+LB Dust Continuum and Molecular Line Maps

Continuum/Line	Frequency (GHz)	Robust	Beam Size	Velocity Resolution (km s^{-1})	Peak Intensity (mJy beam^{-1})	rms Noise (mJy beam^{-1})
1.3 mm continuum	225	−0.5	0.″043 × 0.″036 (−55.°8)	···	5.95	0.04
1.3 mm continuum	225	+0.5	0.″084 × 0.″071 (+78.°0)	···	7.10	0.02
$C^{18}O$ ($J = 2 \rightarrow 1$)	219.56035	+1.5	0.″154 × 0.″141 (−82.°6)	0.167	16.2	1.85
SO ($J_N = 6_5 \rightarrow 5_4$)	219.94944	+1.5	0.″155 × 0.″139 (−84.°6)	0.167	19.2	2.19
^{13}CO ($J = 2 \rightarrow 1$)	220.39868	+1.5	0.″146 × 0.″132 (−81.°1)	0.167	31.4	2.33
^{12}CO ($J = 2 \rightarrow 1$)	230.53800	+1.5	0.″166 × 0.″150 (−81.°4)	0.635	92.3	1.01

Note. The values listed here were obtained from the maps using SB+LB observations. Dust continuum maps for all the robust values produced by the eDisk imaging script are shown in Appendix A. SB-only observation maps of the molecular lines in this table are described and shown in Appendix C. The peak intensities of the continuum maps were found by using a 2″ circular aperture around the center position, while for the line maps the same aperture was used but on the channel with the highest intensity. The rms noise values of the continuum maps were found by using a 10″ circular aperture in an emission-free area, while for the line maps the same aperture was used but around the center position on a line-free channel.

and B_ν is the Planck function for the dust temperature $T_{\rm dust}$. We use the integrated flux density of 7.89 mJy from the Gaussian fitting and a distance of 155.5 pc. We adopt a gas-to-dust ratio of 100 for a 1.3 mm dust opacity value of $\kappa_\nu = 0.023\ {\rm cm^2\ g^{-1}}$ (Beckwith et al. 1990). For the dust temperature, we consider two cases. In the first, we use a $T_{\rm dust}$ of 20 K, which is a typical value adopted in studies of low-mass star formation (e.g., Jørgensen et al. 2009; Tobin et al. 2015). In order to give a more direct comparison of disk masses between sources in our eDisk sample, which have a wide range of protostellar luminosities, we also adopt a temperature distribution that scales with the bolometric luminosity ($L_{\rm bol}$) of the source. We use the following relation:

$$T_{\rm dust} = 43\ {\rm K}\left(\frac{L}{L_\odot}\right)^{0.25}, \quad (3)$$

which was derived using a grid of radiative transfer models (Tobin et al. 2020). For the measured $L_{\rm bol}$ of $1.4\,L_\odot$ (Ohashi et al. 2023), the resulting dust temperature is calculated to be 47 K. We calculate a (gas+dust) disk mass of $1.7 \times 10^{-3}\,M_\odot$ ($1.8 M_{\rm J}$) for $T_{\rm dust} = 20$ K and $6.1 \times 10^{-4}\,M_\odot$ ($0.6 M_{\rm J}$) for $T_{\rm dust} = 47$ K. If the dust is optically thick, these values would be lower limits.

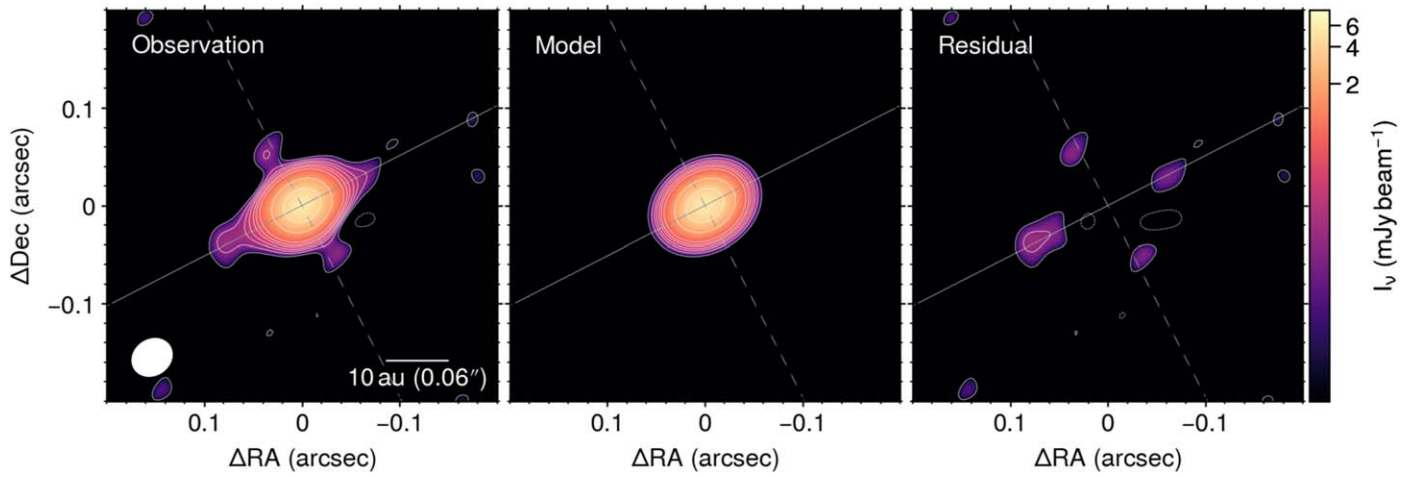

Figure 2. The 2D Gaussian fitting results of IRAS15398. Left: the robust = −0.5 map as shown in Figure 1. Middle: the 2D Gaussian fitting model results. The solid and dashed gray lines indicate the deconvolved position angle of the continuum major and minor axes, respectively. Right: the residual map made by subtracting the model from the observations. The contours are shown in steps (3, 5, 7, 9, 12, 15, 20, 50, 100)$\sigma_{\rm rms}$, where $\sigma_{\rm rms}$ is the rms noise in the robust = −0.5 map.

Table 3
2D Gaussian Fitting and Disk Mass

Parameter	Value
Peak Position	
R.A. (ICRS)	$15^{\rm h}43^{\rm m}02\overset{\rm s}{.}232$
decl. (ICRS)	$-34°09'06\overset{''}{.}96$
Deconvolved Size	
$\theta_{\rm maj}$ (mas)	28.5 ± 0.7
$\theta_{\rm min}$ (mas)	18.1 ± 0.6
$\theta_{\rm pa}$ (deg)	117.1 ± 2.7
i (deg)	50.7 ± 2.0
Peak Intensity and Integrated Flux Density	
$I_\nu^{\rm fit}$ (mJy beam^{-1})	5.86 ± 0.04
$S_\nu^{\rm fit}$ (mJy)	7.89 ± 0.09
(Gas + Dust) Disk Mass	
$M_{\rm disk}$ ($M_\odot$)	
- for $T_{\rm dust}$ = 20 K	1.69×10^{-3}
- for $T_{\rm dust}$ = 47 K	6.14×10^{-4}

Note. These results were obtained using the robust = −0.5 dust continuum map.

3.2. Molecular Lines

The high-resolution (SB+LB) ^{12}CO (2−1), C^{18}O (2−1), ^{13}CO (2−1), and SO ($6_5 - 5_4$) integrated intensity and intensity-weighted velocity maps of IRAS15398 are shown in Figures 3 and 4, respectively. Both the integrated intensity and intensity-weighted velocity maps are made using the *bettermoments* package (Teague & Foreman-Mackey 2018; Teague 2019). The centroid velocity is chosen to be 5.2 km s^{-1} for the intensity-weighted velocity maps (Yen et al. 2017a). The emission above 3σ in the data cubes was masked, along with the emission above 3σ in the integrated intensity maps. The angular resolution of ∼150 mas (23 au at 155.5 pc) is ∼3 times better resolution than the previous Band 6 observations reported in Yen et al. (2017a) and at least ∼1.3 times better than the more recent Band 6 observations reported by Okoda et al. (2018, 2021) and Okoda et al. (2023). The estimated rms values of the ^{12}CO, C^{18}O, ^{13}CO, and SO integrated intensity maps are 4.5, 1.2, 2.3, and 1.9 mJy beam^{-1} km s^{-1}, respectively. Channel maps of the SB +LB molecular line data are shown in Appendix B, with their prominent features described in this section. SB-only maps of the aforementioned molecules are shown in Appendix C and are also briefly described in this section in comparison with their respective SB+LB maps. Several other molecular lines are also targeted by the eDisk program, including three transitions of H_2CO ($3_{0,3} - 2_{0,2}$, $3_{2,2} - 2_{2,1}$, $3_{2,1} - 2_{2,0}$), four transitions of c-C_3H_2 ($6_{0,6} - 5_{1,5}$, $6_{1,6} - 5_{0,5}$, $5_{1,4} - 4_{2,3}$, $5_{2,4} - 4_{1,3}$), and single transitions of CH_3OH ($4_2 - 3_1$ E), DCN (3−2), and SiO (5−4). In this paper, we focus on the highest spectral resolution CO and SO isotopologue lines.

3.2.1. ^{12}CO (2–1)

The large-scale ^{12}CO emission is shown in Figures 3(a) and 4(a). The outflow is clearly traced by ^{12}CO and exhibits a slight bend downward on the northeastern redshifted side and upward on the southwestern blueshifted side. This is consistent with the precessing outflow previously interpreted by Vazzano et al. (2021). Additionally, it is visually clumpy in the integrated intensity map. There is enhanced emission in the outer cavities near the source, especially on the upper side of the redshifted outflow and on the lower side of the blueshifted outflow (Figure 3(a)). There is a slightly blueshifted patch of emission to the southeast at ∼1000 au and northwest at ∼700 au (Figure 4(a)). In the ^{12}CO channel map, the southeast patch is seen in between 3.50 and 4.77 km s^{-1} and seems to increase in velocity as the distance increases from the source (Figure B1). The northwest patch appears in many of the blueshifted channels and is aligned parallel to the redshifted outflow. The redshifted outflow shows a mixture of red- and blueshifted emission, hinting that the outflow is more likely in the plane of sky. The outflows are offset from the direction perpendicular to the disk. The position angles of the red- and blueshifted outflows were previously found to be $64\overset{\circ}{.}9 \pm 0\overset{\circ}{.}2$ and $232\overset{\circ}{.}0 \pm 0\overset{\circ}{.}2$, respectively (Vazzano et al. 2021). This leads to offsets of $117\overset{\circ}{.}1 - 64\overset{\circ}{.}9 = 52\overset{\circ}{.}2$ for the redshifted outflow and $232\overset{\circ}{.}0 - 117\overset{\circ}{.}1 = 114\overset{\circ}{.}9$ for the blueshifted outflow from the inferred position angle of the disk, where one would generally expect a ∼90° (perpendicular) offset. This offset could further indicate a possible precessing outflow caused by tidal interactions of a

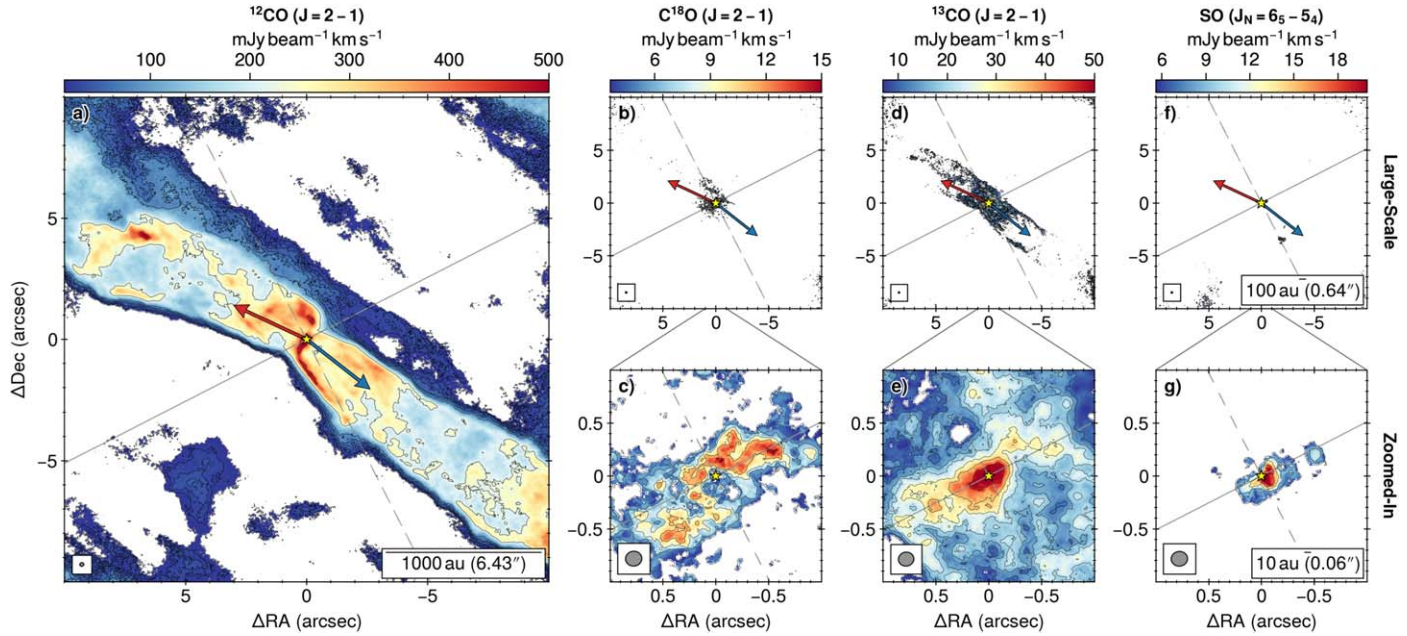

Figure 3. Integrated intensity maps of the representative molecular lines for IRAS15398. Each column is labeled with the respective molecular line. On the left, we show the large-scale structure of ^{12}CO (panel (a)). On the right, we show C^{18}O, ^{13}CO, and SO, with a large-scale view in the top row (panels (b), (d), and (e)) and a zoomed-in view in the bottom row (panels (c), (e), and (g)). The yellow star represents the protostellar position. The beam sizes are shown as the gray circles in the lower left corner of each map, and scale bars are shown in the lower right corner of the ^{12}CO map, as well as the rightmost SO maps for different physical scales. The solid and dashed gray lines indicate the deconvolved position angle of the continuum major and minor axes, respectively. The blue and red arrows represent the overall blue- and redshifted outflow directions found by Vazzano et al. (2021), respectively. The black contours show the integrated intensity in steps (3, 5, 7, 9, 12, 15, 20, 50, 100)$\sigma_{\rm rms}$, where $\sigma_{\rm rms}$ is the rms noise of the respective integrated intensity map.

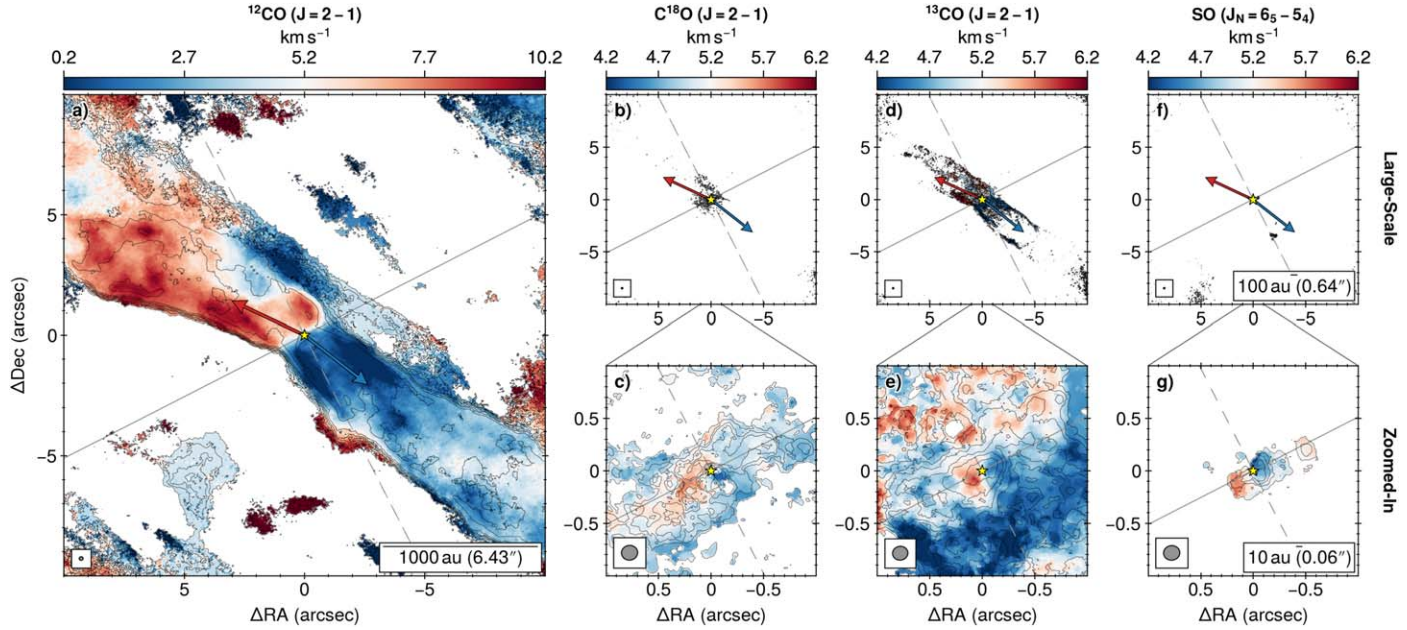

Figure 4. Same as Figure 3, but for the intensity-weighted velocity maps of the representative molecular lines.

binary companion or asymmetric infall reorienting the angular momentum axis of the disk (e.g., Lee 2020). Compared to the SB-only map (Figures C1(a) and C2(a)), the overall structure is the same. There are clumpy portions, and the extended structure to the southeast is also present.

3.2.2. $C^{18}O$ (2–1)

The large-scale view of C^{18}O is shown in Figures 3(b) and 4(b), while a zoomed-in view of the inner region is shown in Figures 3(c) and 4(c). The C^{18}O emission is more centralized, with an asymmetric ring-like structure surrounding the central source (Figures 3(b) and (c)). There is a clear velocity gradient in the velocity map (Figure 4(c)) going from northeast (red) to southwest (blue), which is similar to the continuum minor axis and almost perpendicular to the ^{13}CO and SO velocity gradients. The C^{18}O velocity gradient then twists toward the counterclockwise direction and becomes more aligned to the continuum major axis at larger scales around the disk. The

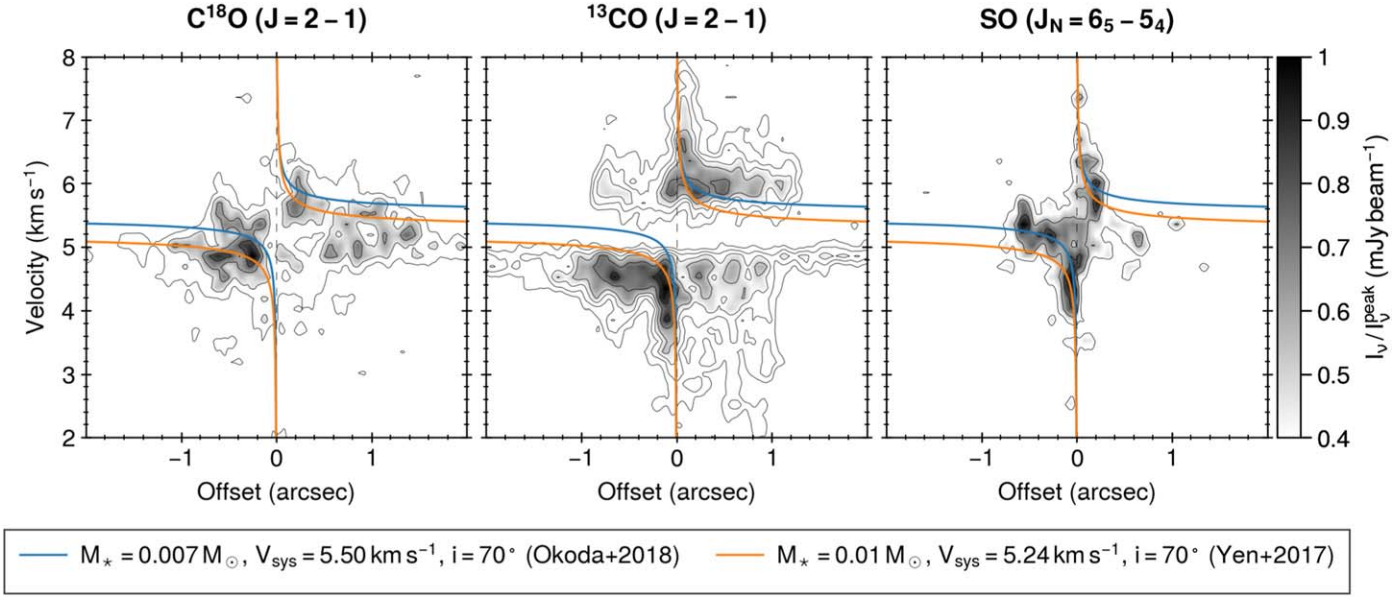

Figure 5. PV diagrams of $C^{18}O$ (left), ^{13}CO (middle), and SO (right). All cuts were made with a width of 1 beam. The offset axis goes from west (negative) to east (positive). The color bar scale is normalized by the peak intensity ($I_\nu^{\rm peak}$). The emission is also shown with black contours in steps (3, 5, 7, 9, 12, 15, 20, 50, 100)$\sigma_{\rm rms}$, where $\sigma_{\rm rms}$ is the rms noise of the respective PV map. The blue and orange lines represent the Keplerian curves for the protostellar masses, system velocities, and disk inclination angles reported by Okoda et al. (2018) and Yen et al. (2017a), respectively.

$C^{18}O$ channel map shows that the emission faintly traces the bipolar outflows, as well as some faint extended emission at low velocities perpendicular to the outflows (Figure B2). In the SB-only integrated intensity map (Figures C1(b) and (c)), the asymmetric structure is not as clear as in the SB+LB maps. In the intensity-weighted velocity maps, the faint extended emission is more clearly seen (Figure C2(b)). Additionally, the overall velocity gradient around the central source appears more consistent with the continuum major axis (Figure C2(c)).

3.2.3. ^{13}CO (2–1)

The large-scale view of ^{13}CO is shown in Figures 3(d) and 4(d), while the inner region is shown in Figures 3(e) and 4(e). The ^{13}CO emission traces parts of the outflow cavity and inner structure around the protostar (Figures 3(d) and (e)). There is a clear velocity gradient around the source position that is consistent with the continuum major axis, indicating rotation around the center. The ^{13}CO channel map shows a similar structure to $C^{18}O$, with the outflows and perpendicular extended emission both present (Figure B3). In the ^{13}CO channel map (Figure B3), the southeast structure is clearly seen between 4.19 and 4.85 km s^{-1}, while the northwest structure is present from 4.52 to 4.85 km s^{-1}. Similar to ^{12}CO, the velocity increases as the emission moves farther away from the source. This is clearer in the southeast structure. In the SB-only maps (Figures C1(d) and (e)), the extended structures perpendicular to the outflow are clear and blueshifted from the centroid velocity. The southeast structure extends out ∼800 au and reaches the blueshifted patch of ^{12}CO previously mentioned. The structure to the northwest is shorter and reaches out to a few hundred au. The extended structures are clearer in ^{13}CO than in $C^{18}O$. In the SB+LB maps, these extended structures are resolved out.

3.2.4. SO (6_5–5_4)

The large-scale view of SO is shown in Figures 3(f) and 4(f), while the inner region is shown in Figures 3(g) and 4(g). The SO emission is compact and mostly located around the center near the protostellar position (Figures 3(f) and (g)). SO emission can be enhanced in and around the protostellar disk owing to either accretion shocks from the infalling material (e.g., Ohashi et al. 2014; Sakai et al. 2014, 2017; van Gelder et al. 2021) or MHD disk winds (Tabone et al. 2017). There is a clear velocity gradient that is consistent with both ^{13}CO and the continuum major axis (Figure 4(g)). A higher excited transition of SO ($J_N = 7_6 \rightarrow 6_5$) was previously shown to trace rotation associated with a protostellar disk (Okoda et al. 2018). A small, offset patch of redshifted emission is seen in the disk plane, which could be associated with an accretion shock or the infalling envelope. There is a blueshifted patch of SO emission that is coincident with the previously mentioned ^{12}CO patch in the southeast at ∼1000 au. In addition, there is a small patch of SO at the bottom edge of the blueshifted outflow, which likely traces a shocked region in the outflow. The SB-only large-scale maps show the extended feature and the outflow shock more clearly (Figures C1(f) and C2(f)), while the zoomed-in map also shows a velocity gradient similar to that in the SB+LB map (Figures C1(g) and C2(g)).

4. Analysis

4.1. Position–Velocity Diagrams

Our high angular resolution data allow us to investigate the Keplerian disk in this source at smaller scales than in previous studies. We make some initial PV diagrams to get an overview of the velocity structure and look for lines that show a Keplerian rotation signature. We investigate $C^{18}O$, ^{13}CO, and SO by making PV cuts with widths of 1 beam across the continuum disk major axis (PA = 117.°1) as measured from the dust continuum fitting. The resulting PV diagrams are shown in Figure 5.

The $C^{18}O$ emission takes a diamond shape, with emission in all four quadrants of the PV diagram (Figure 5, left panel). This is indicative of infall-dominated motions (e.g., Ohashi et al. 1997;

Harsono et al. 2015). The PV diagram of ^{13}CO is much more complicated (Figure 5, middle panel). The red- and blueshifted velocity signature seen in the center of the integrated intensity map (Figure 4(e)) likely corresponds to some of the emission seen in the upper right and lower left quadrants, which could be tracing infalling and rotational components of the system. However, there are several high-velocity structures in all four quadrants, which are likely due to contamination by the outflow kinematics. The lack of emission at velocities around the line center is likely due to filtering out by the high angular resolution. The PV structure in the SO map seems the most promising to trace a possible disk rotation signature around the protostar (Figure 5, right panel). The overall emission mainly shows up in the upper right and lower left quadrants of the PV diagram. This is expected for rotational motions, where faster rotation would shift the emission peaks to smaller offsets (e.g., Harsono et al. 2015). This PV structure is also consistent with a higher transition of SO (at ∼261 GHz) that was previously analyzed by Okoda et al. (2018).

We briefly compare the PV structures in Figure 5 to Keplerian rotation curves using previous protostellar mass estimations (Yen et al. 2017a; Okoda et al. 2018). We assume the system velocity to be 5.24 km s^{-1} as previously estimated by Yen et al. (2017a) using C^{18}O. It is worth noting that Okoda et al. (2018) employ a higher system velocity of 5.5 km s^{-1} for their Keplerian analysis of SO. In our case, the overall PV structure of C^{18}O and ^{13}CO is more consistent with the lower value. The Keplerian curves seem to match well with the higher-velocity SO emission near the source. As for C^{18}O and ^{13}CO, it is not clear whether the emission corresponds to the rotation curves in the same high-velocity region near the source. Thus, SO seems to be the most promising for studying the dynamics of the protostellar disk in IRAS15398.

4.2. PV Analysis with SLAM

We employ the rotation curve fitting tool from the Spectral Line Analysis/Modeling (SLAM) Python package,[20] which uses Markov Chain Monte Carlo (MCMC) sampling to fit a single or double power-law profile to the emission in the PV diagram (Aso & Sai 2023). Here we present a brief overview of the fitting procedure and methodology and refer the reader to Ohashi et al. (2023) for a complete description (see also Aso et al. 2015; Aso & Machida 2020; Sai et al. 2020). In the case of a single power law, the velocity is described by

$$v = V_b\left(\frac{r}{R_b}\right)^{-p}, \tag{4}$$

where R_b is an arbitrarily chosen "break" radius at a fixed velocity V_b and p is the power-law index. The double power-law case describes the velocity as

$$v = \begin{cases} V_b\left(\frac{r}{R_b}\right)^{-p_{\rm in}} & (r \leqslant R_b) \\ V_b\left(\frac{r}{R_b}\right)^{-p_{\rm out}} & (r > R_b) \end{cases} \tag{5}$$

where $p_{\rm in}$ and $p_{\rm out}$ are the inner and outer power-law indices, respectively. Instead of strictly defining $p_{\rm out}$, SLAM instead implements the variable dp, which is simply the change in power-law indices ($dp = p_{\rm out} - p_{\rm in}$). We will describe p and dp, instead of $p_{\rm in}$ and $p_{\rm out}$, for the remainder of the paper to simplify the descriptions between single and double power-law indices. A power-law index of $p \approx 0.5$ represents a Keplerian rotating disk, while $p \approx 1$ represents infalling material with conserved angular momentum. The algorithm finds the edges and ridges of the emission in the PV diagram by cutting along the position and/or velocity axes. One can set an intensity threshold at which to find the edge and ridge points. Changing the threshold mainly affects the edge calculation, as the outermost radius with this value is the edge radius. For the ridge calculation, the mean is found using data above the threshold. The edge and ridge points are then separately fit with the power-law function to find the best parameters. The dynamical mass can then be estimated via the Kepler mass by

$$M = v^2 r / G / \sin^2 i, \tag{6}$$

where G is the gravitational constant and i is the source inclination angle. The mass can be interpreted as the dynamical protostellar mass ($M_\star$) when $p \approx 0.5$, and the true protostellar mass would then be somewhere between the break masses, M_b, estimated from the edge (upper mass limit) and ridge (lower mass limit) methods. If p is not Keplerian but close to it, M_b tells us a reasonable range of the protostellar mass. Additionally, the break radius only represents the disk radius when fitting the double power-law function. In the case of a single power law, the break radius is arbitrarily chosen from within the derived points, usually where the cuts for both position and velocity meet.

In the following sections, we describe multiple different PV diagram fittings of the SO emission using single and double power-law profiles from SLAM. Our high-resolution data will provide the first PV diagram fitting of the IRAS15398 protostellar disk, as the previous observations by Yen et al. (2017a) did not resolve the disk. Fitting the PV diagram, especially for protostars with small disks, may not be very straightforward, which is shown by our multiple fitting attempts. We quantify the "goodness of fit" to assess which models best quantify the current data. Several parameters are kept the same among the different fits. We set the distance to IRAS15398 as 155.5 pc and the inclination angle to 50.°7, as estimated by the 2D Gaussian fitting in Section 3.1. We use a 5σ threshold, where the rms of the PV diagram is measured to be $\sigma = 1.55$ mJy beam^{-1}. A lower threshold of 3σ was also tested; however, the reduced chi-squared was higher than when using a 5σ threshold. We explore values less than 2 $M_\odot$ for the central protostellar mass, which is the expected limit given the evolutionary stage of the source and its luminosity. The SLAM fitting results are presented in Table 4. Additionally, we show the results in both PV and radius–velocity (RV) space in Figures 6 and 7, respectively.

4.2.1. Single Power Law

Initial: We begin with an initial SLAM fitting using the single power-law function (Equation (4)). The full PV extent of the SO emission is utilized by setting the position range

[20] The Spectral Line Analysis/Modeling (SLAM) tool is publicly available at https://github.com/jinshisai/SLAM. This tool was developed for the eDisk large program to derive dynamical protostellar masses.

Table 4
SLAM Fitting Results for SO ($J_N = 6_5 \rightarrow 5_4$)

Fitting Description	Fitting Method	R_b (au)	p	dp	V_{sys} (km s^{-1})	M_b ($M_\odot$)	$\bar{\chi}^2$
Initial	Edge	$41.39^{+1.12}_{-1.13}$	$1.09^{+0.09}_{-0.08}$	⋯	$5.42^{+0.02}_{-0.02}$	0.0299 ± 0.0008	3.8
- $V_{range} = 0.0$–2.0 km s^{-1}, p = free, V_{sys} = free	Ridge	$57.84^{+2.64}_{-2.60}$	$0.81^{+0.03}_{-0.03}$	⋯	$5.47^{+0.01}_{-0.01}$	0.0066 ± 0.0003	6.3
Modified 1	Edge	$23.05^{+1.81}_{-1.77}$	$0.85^{+0.28}_{-0.18}$	⋯	$5.37^{+0.08}_{-0.05}$	0.053 ± 0.004	1.6
- $V_{range} = 0.6$–2.0 km s^{-1}, p = free, V_{sys} = free	Ridge	$10.38^{+0.93}_{-0.90}$	$0.64^{+0.21}_{-0.11}$	⋯	$5.44^{+0.08}_{-0.05}$	0.024 ± 0.002	1.4
Modified 2	Edge	$19.40^{+1.12}_{-1.10}$	0.5	⋯	$5.30^{+0.02}_{-0.02}$	0.045 ± 0.003	1.8
- $V_{range} = 0.6$–2.0 km s^{-1}, p = fixed, V_{sys} = free	Ridge	$9.68^{+0.66}_{-0.64}$	0.5	⋯	$5.40^{+0.03}_{-0.03}$	0.022 ± 0.002	1.2
Modified 3	Edge	$24.12^{+1.37}_{-1.50}$	1.0	⋯	$5.40^{+0.04}_{-0.04}$	0.055 ± 0.003	1.6
- $V_{range} = 0.6$–2.0 km s^{-1}, p = fixed, V_{sys} = free	Ridge	$11.11^{+0.95}_{-0.98}$	1.0	⋯	$5.57^{+0.06}_{-0.05}$	0.026 ± 0.002	2.3
Modified 4	Edge	$21.30^{+49.08}_{-7.31}$	$0.71^{+0.15}_{-0.32}$	$0.36^{+0.49}_{-0.26}$	$5.40^{+0.02}_{-0.02}$	0.06 ± 0.1	2.4
- $V_{range} = 0.2$–2.0 km s^{-1}, p = free, dp = free, V_{sys} = free	Ridge	$19.23^{+41.40}_{-13.39}$	$0.74^{+0.05}_{-0.022}$	$0.26^{+1.29}_{-0.20}$	$5.46^{+0.01}_{-0.01}$	0.014 ± 0.04	8.3
Modified 5	Edge	$18.25^{+4.82}_{-3.28}$	0.5	0.5	$5.39^{+0.02}_{-0.02}$	0.07 ± 0.03	14.4
- $V_{range} = 0.2$–2.0 km s^{-1}, p = fixed, dp = fixed, V_{sys} = free	Ridge	$21.87^{+1.44}_{-1.60}$	0.5	0.5	$5.45^{+0.01}_{-0.01}$	0.016 ± 0.002	4.7

Note. R_b is the break radius, p is the power-law index (or inner power-law index for the double power-law function), dp is the change in the double power-law index between the inner and outer functions, V_{sys} is the systemic velocity, M_b is the dynamical mass at the break radius, and $\bar{\chi}^2$ is the reduced chi-squared of the fit. For the single power-law fittings, the break radius is arbitrarily chosen from within the derived points. For the double power-law fitting, $p = p_{in}$ and $dp = p_{out} - p_{in}$ and the break radius is where the power law transitions from inner to outer. The uncertainties reported are the 16th and 84th percentiles of the posterior distributions in the MCMC fitting.

parameter from 0 to 100 au and the velocity range parameter from 0 to 2 km s^{-1}. Both position and velocity cuts are used to derive the edge and ridge points for fitting. The power-law index and systemic velocity are kept as free variables. The results of our initial fitting are shown in Figures 6(a) and 7(a). The derived data points from the initial SLAM fit show no visual break in the slope, where one might expect a power-law transition from infalling material ($p \sim 1$) to disk ($p \sim 0.5$). This motivates our initial use of a single power-law function for fitting the data. At radii <10 au, the slope of the points may start to flatten out around 0.″3, but the lack of points at these smaller radii due to the angular resolution cannot confirm this. Curiously, there is one very low-velocity point at ∼100 au. Including the systemic velocity as a free parameter gives a value of ∼5.45 km s^{-1}. The best-fit power-law indices from the edge and ridge fits are both closer to $p \sim 1$, which indicates infalling material with conserved angular momentum. However, this result could be influenced by the low-velocity points farther away from the source, as well as the choice of the system velocity. The reduced chi-squared ($\bar{\chi}^2$) values of the fits are 3.8 and 6.3 for the edge and ridge methods, respectively. It is important to see how these variables affect the overall fitting and whether it is possible to recover a Keplerian power-law profile.

4.2.2. Modified Single Power Law

Modified 1: We first modify our initial SLAM fitting by increasing the lower limit of the velocity range to 0.6 km s^{-1}, in order to only include the high-velocity points in our fit. Additionally, we only fit along the velocity axis since peak positions in the PV emission are at similar offsets at these higher velocities. All of the other parameters remain the same. The results of this first modified fitting are shown in Figures 6(b) and 7(b). The errors in the fitting results for the power-law index and system velocity are larger owing to the limited number of data points at higher velocities included in the fit. The best-fit systemic velocity is ∼5.4 km s^{-1}. This is slightly lower but still consistent with the value derived from the initial fit. Overall, the power-law index between the edge and ridge methods is lower at around $p \sim 0.75$. The power-law index from the initial fit is within the upper error bound for both the edge and ridge fits. On the other hand, the lower error bounds are now significantly closer to Keplerian rotation. Thus, it is difficult to make a concrete conclusion on whether the emission is related to the infalling envelope or a Keplerian disk. The $\bar{\chi}^2$ of both the edge and ridge is lower than the initial fit at 1.6 and 1.4, respectively, indicating a better overall fit than the initial.

Modified 2 and 3: Since the power-law indices in our Modified 1 fit are somewhere between infall and Keplerian rotation, we fix the power-law indices to both scenarios ($p = 1.0$ and $p = 0.5$) to see how the $\bar{\chi}^2$ is affected in order to narrow down which scenario is more likely. We first run SLAM with a fixed $p = 0.5$ for Keplerian rotation (Modified 2). The $\bar{\chi}^2$ for the ridge method is 1.2, which is slightly lower than but fairly consistent with the value in the Modified 1 ridge fit. This is due to the power-law index from the Modified 1 ridge estimate being closer to 0.5. In the edge method, the $\bar{\chi}^2$ is 1.8 and also consistent with but slightly higher than that in the Modified 1 edge fit. In contrast, when running SLAM with a fixed $p = 1.0$ for infalling envelope (Modified 3), the ridge method $\bar{\chi}^2$ becomes a much higher value of 2.3. This shows that the ridge is tracing Keplerian rotation rather than infall, giving a lower limit on the protostellar mass of $0.022 \pm 0.002\,M_\odot$. The $\bar{\chi}^2$ for the edge method is actually the same value of 1.6 as in the Modified 1 fit. Thus, we cannot distinguish whether the edge follows Keplerian rotation or infall to constrain the protostellar mass upper limit. This could be due to insufficient angular resolution smearing the PV emission at the edge. The single power-law fittings do not directly give a disk radius, since the break radius from these fits is arbitrarily chosen to be within the derived points. However,

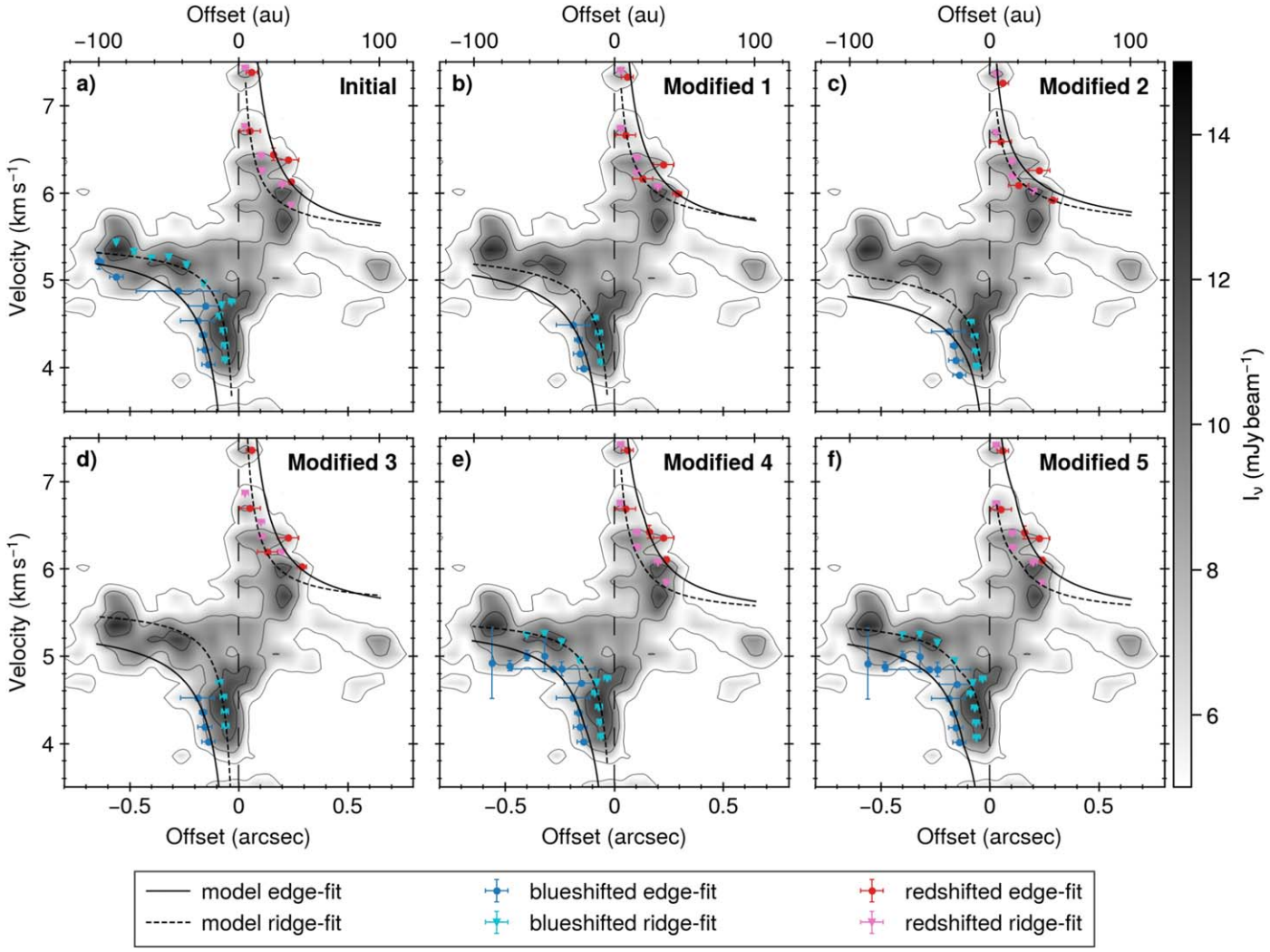

Figure 6. The PV plots of the SLAM fitting results for SO. The red and blue circles represent the red- and blueshifted points fit with the edge method, respectively, while the magenta and cyan triangles represent the red- and blueshifted points fit with the ridge method, respectively. The black solid and dashed lines show the best-fit edge and ridge models, respectively. The contours in the PV map are shown in steps (3, 5, 7, 9, 12, 15, 20, 50, 100)$\sigma_{\rm rms}$, where $\sigma_{\rm rms}$ is the rms noise in the PV map.

we can infer a lower limit of the protostellar disk radius using the outermost point of our ridge fit, which is 31.2 ± 2.4 au.

4.2.3. Double Power Law

Modified 4 and 5: The expected transition from infalling material to a Keplerian rotating disk provides a physical motivation to fit the observed PV diagrams with a double power-law function (Equation (5)). Although a break in the data points is not clear, it is worth investigating whether we can recover a potential protostellar disk radius and compare the $\bar{\chi}^2$ values to the single power-law fits. The first double power-law fit (Modified 4) leaves p (or $p_{\rm in}$) and dp as free parameters. Overall the inner and change in power-law indices are $p \sim 0.73$ and $dp \sim 0.31$, respectively ($p_{\rm out} \sim 1.04$), which are very reasonable values and indicate that the outer power-law index is more consistent with infall, while the inner power-law index is slightly higher than Keplerian. However, the $\bar{\chi}^2$ values of 2.4 and 8.3 for the edge and ridge, respectively, are much larger than the single power-law fits. This is also apparent in the Modified 5 fit, where p and dp are both fixed to 0.5 ($p_{\rm out} = 1.0$) and the $\bar{\chi}^2$ are also much higher at 14.4 and 4.7 for the edge and ridge, respectively. Comparing the two power-law fits, we do see a somewhat similar trend of the $\bar{\chi}^2$ for the edge and ridge as seen in the previous single power-law fits. The ridge method produces a lower $\bar{\chi}^2$ when p and dp are both fixed and the inner power law is Keplerian, whereas the edge $\bar{\chi}^2$ is much higher for the fixed values and less when left free and the power law is steeper than Keplerian. This really demonstrates the difficulty in fitting PV diagrams of the smallest protostellar disks, and caution should be taken when interpreting results.

5. Discussion

5.1. A Very Low Mass Protostar and Disk

The single power-law ridge fittings suggest the presence of a Keplerian disk. This constrains the lower limit of the dynamical protostellar mass of IRAS15398 to be $0.022 \pm 0.002\,M_\odot$. Unfortunately, the edge method in the single power-law fits does not clearly indicate the existence of a Keplerian disk, since we cannot distinguish whether the power-law index is closer to 0.5 (Keplerian) or 1.0 (infall). Insufficient angular resolution could cause smearing near the edges of the PV diagram emission, making it difficult to recover the power-law index. Because of the unclear results of the PV edge in the single power-law fittings, it is not easy for us to estimate an

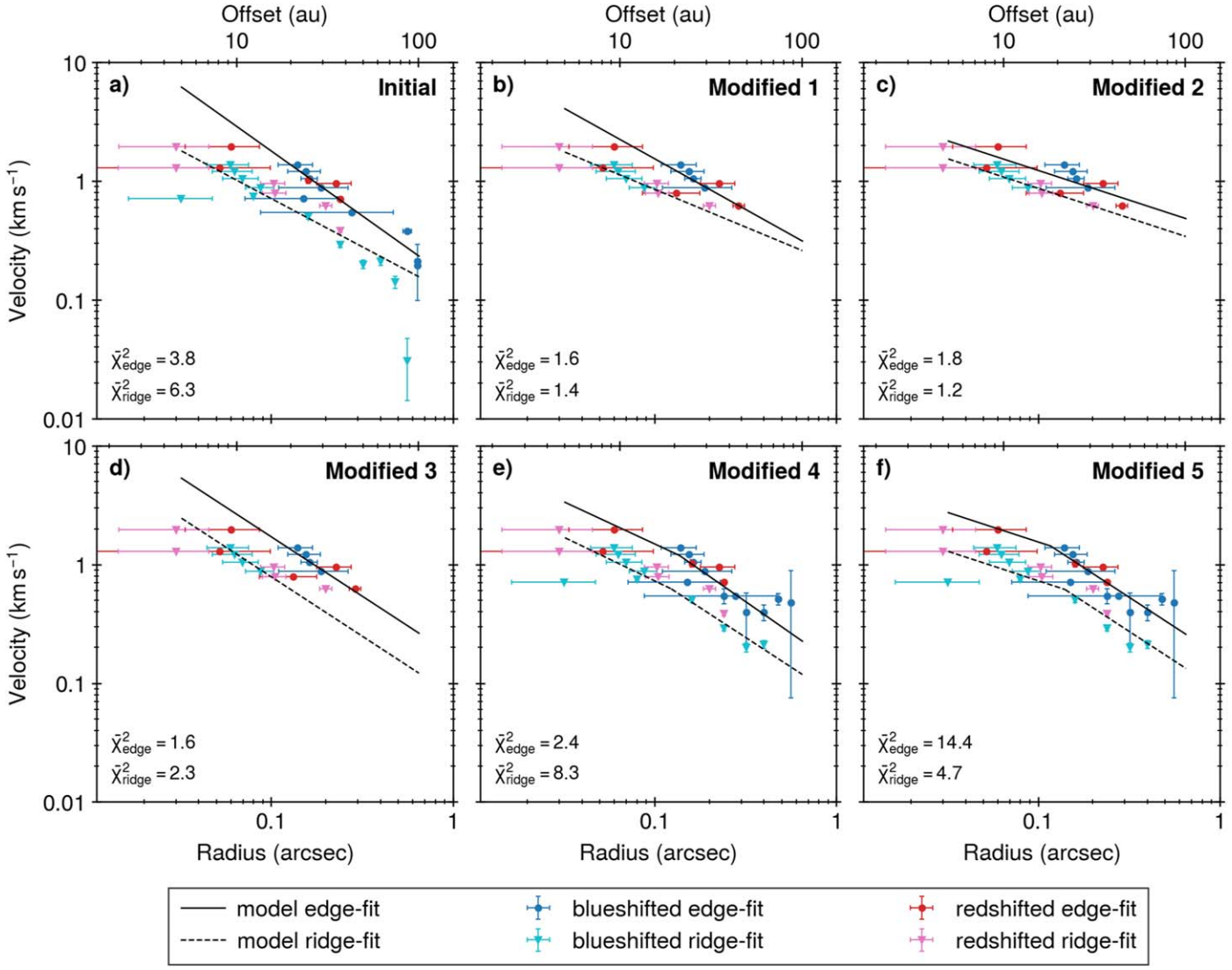

Figure 7. The RV plots of the SLAM fitting results for SO. The colored points and black lines have the same meaning as in Figure 6. The best-fit power-law equations are shown in the lower left corner.

upper limit of the stellar mass. Based on the outline of the edge contour of the PV diagram, we can conservatively estimate an upper-limit protostellar mass to be $\sim 0.1\,M_\odot$. The double power-law fits are not used to determine the protostellar mass and disk radius owing to the lack of clear break in the derived points used for fitting and the higher overall $\tilde{\chi}^2$ values. The very low mass indicates that IRAS15398 is likely in its infancy, which is also consistent with approximate ages ($\sim$1000 yr) derived from the dynamical timescale of the protostellar outflows (Bjerkeli et al. 2016b; Vazzano et al. 2021) and the lack of substructures in the dust disk. Earlier studies by Oya et al. (2014) and Yen et al. (2017a) used infalling envelope models to constrain the protostellar mass to be less than $0.09\,M_\odot$ and $0.01^{+0.02}_{-0.01}\,M_\odot$, respectively. It should be noted that the upper limit by Yen et al. (2017a) is under the assumption that the infall is freefall, and if the infall is actually slower than freefall, this estimated mass would be a lower limit (see also Ohashi et al. 2014; Aso et al. 2015). These studies did not clearly detect a Keplerian rotation signature, but their derived protostellar masses are consistent with this study. Okoda et al. (2018) infer Keplerian rotation around a protostellar mass of $0.007^{+0.004}_{-0.003}\,M_\odot$ using a by-eye comparison to the molecular emission from their SO ($J_N = 7_6 \rightarrow 6_5$) data. The beam size of their SO data is $\sim$1.5 times larger than ours at $0\farcs22 \times 0\farcs16$ with an rms noise $\sim$1.8 times higher at 4 mJy beam^{-1} at a similar velocity resolution. Since the true protostellar mass likely lies between the edge and ridge fittings of the PV diagram, their comparison to the ridge provides only a lower limit on the protostellar mass. Additionally, Okoda et al. (2018) employ a disk inclination angle of 70° in their comparison, which is $\sim$20° higher than our estimate of 50.°7 from the 2D Gaussian fitting of the dust continuum. Adjusting the previous mass value for our new inclination angle increases the mass to $\sim 0.01\,M_\odot$, which is still consistent with our result as a lower limit. Overall, the method used for deriving the protostellar mass is inherently different. Okoda et al. (2018) perform a by-eye comparison using the ridge of the PV emission, which seemingly does match well to their PV structure. If a higher velocity of 5.5 km s^{-1} is assumed, then the more extended, lower-velocity emission on the blueshifted side of the PV diagram could be interpreted as being in Keplerian rotation and thus change the resulting protostellar mass estimation when matching by eye. When visually comparing our PV fitting

results in Figure 6, it is somewhat difficult to tell the difference when the power law is Keplerian versus infall. Protostellar mass estimations using the methodology in this paper were tested with numerical simulations of protostellar disk formation at several epochs (Aso & Machida 2020). It was found that the true protostellar mass is likely between mass estimates from both the edge and ridge PV estimations. This means that using only the ridge method could potentially underestimate the true protostellar mass. However, Aso & Machida (2020) also show that the estimated mass from fitting their PV diagram was slightly larger than the actual protostellar mass when $M_\star < 0.4\,M_\odot$, due to the disk mass contributing to the overall rotational velocity in the very early stages. Since the protostellar mass of IRAS15398 is within this limit, it is possible to be slightly overestimated. Compared to other Class 0 sources, the protostellar mass of IRAS15398 is among the smallest (e.g., Tobin et al. 2012; Murillo et al. 2013; Ohashi et al. 2014; Yen et al. 2015b, 2017a; Aso et al. 2017; Maret et al. 2020). An analogous Class 0 protostar with a similarly small protostellar mass is B335 (Yen et al. 2015b). A protostellar mass of $\sim 0.05\,M_\odot$ was suggested from kinematic modeling, even though no Keplerian rotation was detected. These results hinted at the possibility of magnetic braking playing a crucial role in the evolution of B335. This aspect will be discussed more in Section 5.2, where we will compare the magnetic and Keplerian disk properties between IRAS15398 and B335.

The protostellar (gas+dust) disk mass is estimated to be $(0.6\text{–}1.7) \times 10^{-3}\,M_\odot$ (or $0.6M_J$–$1.8M_J$, 191–572 $M_\oplus$) using the integrated flux density from our 2D Gaussian fitting results under an optically thin assumption. If the emission at 1.3 mm is optically thick, the derived disk mass could only be a lower limit. Multiband observations would be useful to constrain the optical depth at these wavelengths. Our assumed gas-to-dust ratio means that the dust-only disk mass is 100 times smaller at roughly 2–6 $M_\oplus$. The recent VANDAM surveys in Perseus and Orion provide estimates on the dust masses (and also dust disk radii; see Section 5.2) in a large sample of Class 0 sources (Segura-Cox et al. 2018; Tobin et al. 2020; Sheehan et al. 2022). From a sample of 14 Class 0 disk candidates, Segura-Cox et al. (2018) estimate the range of disk masses to be 0.01–0.46 $M_\odot$, which is a few orders of magnitude higher than the disk mass in IRAS15398. A more comprehensive study by Tobin et al. (2020) was performed that compared the dust disk masses of Class 0/I protostars in Orion to values of Class 0/I protostars in a few other clouds and also a sample of Class II sources. For Class 0 stars in Orion, the mean and median dust disk mass estimates are $25.9^{+7.7}_{-4.0}\,M_\oplus$ and $25.7^{+102.9}_{-6.7}\,M_\oplus$. The Class 0 protostars in Perseus exhibit overall higher mean and median dust disk masses of $376.5^{+220.3}_{-89.5}\,M_\oplus$ and $549.8^{+1149.0}_{-108.4}\,M_\oplus$, respectively. The dust mass is found to systematically decrease over time when compared to the dust disk mass values in Class II sources. For example, in Lupus, the mean and median protoplanetary dust disk masses are $5.08^{+1.78}_{-1.41}\,M_\oplus$ and $3.5^{+15.2}_{-0.8}\,M_\oplus$, respectively (Ansdell et al. 2016). Radiative transfer modeling by Sheehan et al. (2022) has shown that the Class 0 sample of protostars in Orion and previously modeled by Tobin et al. (2020) may have overestimated the dust disk mass, with larger discrepancies in the lower-mass dust disks. Thus, more detailed radiative transfer modeling of the dust continuum in IRAS15398 would be helpful to constrain the dust disk mass available for future planet formation.

5.1.1. Disk-to-stellar Mass Ratio

The disk-to-star mass ratio is used as an indicator of the gravitational stability of a protostar–disk system, where systems with $M_{\rm disk}/M_\star \gtrsim 0.3$ are more unstable (e.g., Lodato & Rice 2004, 2005). Previous surveys indicate typical values of $M_{\rm disk}/M_\star$ to be between 0.001 and 0.1 in more evolved sources (e.g., Manara et al. 2023, and references therein). Using the mean values of the protostellar disk mass ($(0.61\text{–}1.69) \times 10^{-3}\,M_\odot$) and the lower-limit protostellar mass ($0.022\,M_\odot$), the upper limit of the disk-to-star mass ratio is ~0.06. As mentioned previously, this value could be underestimated if the 1.3 mm dust emission is optically thick. However, the value of $M_{\rm disk}/M_\star$ is well within the limit of a gravitationally stable disk.

5.1.2. Mass Accretion Rate

The mass accretion rate onto the protostar can be estimated by

$$\dot{M}_{\rm acc} = \frac{L_{\rm acc} R_\star}{G M_\star}, \tag{7}$$

where $L_{\rm acc}$ is the accretion luminosity, $R_\star$ is the radius of the protostar, and G is the gravitational constant. We take $L_{\rm acc} \approx L_{\rm bol} = 1.4\,L_\odot$ (assuming $L_{\rm acc} \gg L_\star$) to obtain an upper limit on the mass accretion rate, since $L_{\rm bol} = L_{\rm acc} + L_\star$. The radius of the protostar is assumed to be $R_\star = 3\,R_\odot$ (Stahler et al. 1980). Using the lower-limit-derived protostellar mass of $M_\star = 0.022\,M_\odot$ gives an approximate mass accretion rate of $6.1 \times 10^{-6}\,M_\odot\,{\rm yr}^{-1}$, while our conservative upper limit gives $1.3 \times 10^{-6}\,M_\odot\,{\rm yr}^{-1}$. This mass accretion rate is consistent with the most recent estimate of $(0.2\text{–}7.0) \times 10^{-6}\,M_\odot\,{\rm yr}^{-1}$, which was found using a combination of the dynamical timescale of the outflow and protostellar mass (Oya et al. 2014; Bjerkeli et al. 2016b; Okoda et al. 2018). Assuming that the mass accretion rate is constant, we can estimate the age of the protostar by $M_\star/\dot{M}_{\rm acc}$, which yields an age of approximately $(0.4\text{–}7.5) \times 10^4$ yr, which would be a lower limit. However, IRAS15398 was shown to have undergone an accretion burst in the past 100−1000 yr (Jørgensen et al. 2013). This means that the accretion rate is not constant and this method of approximating age is more uncertain. The dynamical ages of the outflows are younger at <1000 yr for both the red- and blueshifted lobes (Bjerkeli et al. 2016b; Vazzano et al. 2021), which could also be a consequence of the accretion burst.

Early theoretical modeling predicts that a typical mass accretion rate of protostars lies somewhere between 10^{-6} and $10^{-5}\,M_\odot\,{\rm yr}^{-1}$ (Hartmann et al. 1997), while magnetohydrodynamic (MHD) simulations predict values between 10^{-7} and $10^{-4}\,M_\odot\,{\rm yr}^{-1}$, with higher mass accretion rates at earlier times in the simulations (e.g., Machida & Matsumoto 2012). This further points toward IRAS15398 being a younger protostar since its mass accretion rate is on the higher end of values predicted from simulations.

5.1.3. A Proto–Brown Dwarf Candidate?

The upper mass limit of a brown dwarf is $\sim 0.075\,M_\odot$ (Hayashi & Nakano 1963; Kumar 1963a, 1963b; Burrows et al. 1997).

Since the protostellar mass of IRAS15398 is currently within this regime, it is interesting to discuss the possibility of whether IRAS15398 will become massive enough to sustain the nuclear fusion of hydrogen in its core. The envelope mass around IRAS15398 has been previously estimated to be between 0.5 and 1.2 $M_\odot$ (Kristensen et al. 2012; Jørgensen et al. 2013). The protostellar core-to-star efficiency is estimated to be ∼30% from both observations of starless cores and numerical simulations (Enoch et al. 2008; Offner & Chaban 2017). This efficiency would give a final lower-limit stellar mass estimation of 0.15 $M_\odot$ for IRAS15398, well above the mass limit of a brown dwarf.

5.2. An Extremely Small Protostellar Disk

The lower limit of the protostellar gas disk radius is 31.2 ± 2.4 au. A previous upper limit of the disk radius was found to be 20^{+50}_{-20} au by Yen et al. (2017a), which is within the error of our estimate. The gas disk radius in IRAS15398 is comparable to, but on average smaller than, that of other kinematically detected disks. The study by Yen et al. (2017a) looks at the properties of several Class 0/I protostars with Keplerian disks. The gas disk radii in their comparison range from 3 to 150 au in the Class 0 stage. The protostellar disk is expected to continue to grow as more material and angular momenta from the natal, protostellar envelope collapse toward the central region. From a theoretical perspective, small Keplerian disks could indicate efficient magnetic braking of the infalling material (Allen et al. 2003; Hennebelle & Fromang 2008; Mellon & Li 2008). The parsec-scale magnetic field in IRAS15398 has been previously studied using SOFIA polarization observations (Redaelli et al. 2019). They conclude that the core is strongly magnetized with a uniform-to-turbulent magnetic ratio of 0.27. Additionally, the overall magnetic field direction appears well aligned to the outflow direction. Numerical MHD simulations have inversely found that increasing the misalignment between the magnetic field and rotation axis can help to overcome magnetic braking and promote disk formation (e.g., Hennebelle & Ciardi 2009; Joos et al. 2012; Krumholz et al. 2013; Li et al. 2013; Hirano et al. 2020). Thus, this alignment could indicate more efficient magnetic braking, which would inhibit the growth of a large, protostellar disk.

The dust disk radius is taken to be the 2σ width of the deconvolved major axis ($\mathrm{FWHM_{maj}} = 2.355\sigma$) of our 2D Gaussian continuum fitting, which is 3.82 au. In the aforementioned VANDAM survey of Perseus, the dust disk radii ranged between 10.5 and 42.2 au (Segura-Cox et al. 2018). In Orion, the mean and median dust disk radii were found to be $44.9^{+5.8}_{-3.4}$ and $48.1^{+79.6}_{-24.5}$ au, respectively (Tobin et al. 2020). These values are consistently larger than those of the dust disk in IRAS15398, possibly hinting at other mechanisms, like environment effects, that are keeping its dust disk small.

5.2.1. Dust versus Gas Disk Radius

Small dust disks could be a signpost of the radial drift of dust grains as they grow in size and decouple from the gas disks. Discrepancies between the dust and gas disk radii have been observed in more evolved protoplanetary disks (e.g., Panić et al. 2009; Andrews et al. 2012; de Gregorio-Monsalvo et al. 2013; Ansdell et al. 2018; Trapman et al. 2020). Recent work by Ansdell et al. (2018) has revealed that the radii of gas disks were ∼1.5–3.0 times those of the dust disks in their sample of 22 protoplanetary disks in Lupus. We report that the gas disk radius in IRAS15398 is >8 times larger than the dust disk radius, which is significantly larger than those of later-stage disks. In the early, deeply embedded protostellar disk stage, there are currently no studies that have investigated this before the eDisk program. However, if planet formation begins in these early stages, as suggested by substructure formation in a few Class I protostars (ALMA Partnership et al. 2015; Sheehan & Eisner 2018; Segura-Cox et al. 2020; Yamato et al. 2023), then this value could be essential for constraining the dust growth and radial drift in Class 0/I protostars. It should be noted that observed differences in gas and dust disk radii could also be observed owing to the optical depth effects (e.g., Facchini et al. 2017). Further modeling to constrain the optical depths is needed to disentangle these scenarios.

5.2.2. Specific Angular Momentum

The specific angular momentum can be calculated via

$$j = \sqrt{GM_\star R_d}\,, \tag{8}$$

where the lower-limit gas disk radius, $R_d \geqslant 31.2$ au, is used. At the lower limit of the gas disk, the specific angular momentum is found to be 1.2×10^{-4} km s^{-1} pc. Using our conservative upper limit of 0.1 $M_\odot$ and the upper error limit gas disk radius $R_d \approx 70$ au from Yen et al. (2017a), the maximum specific angular momentum is 3.8×10^{-4} km s^{-1} pc. Previous values of the specific angular momentum found at larger scales of 140 and 600 au were found to be $\sim 7 \times 10^{-5}$ km s^{-1} pc and $\sim 1 \times 10^{-4}$ km s^{-1} pc, respectively (Yen et al. 2017a).

While the uncertainty from the mass range is so large, the specific angular momentum seems to increase at smaller radii near the disk. One would expect the specific angular momentum to increase near the disk owing to the dependence on radius. In the inside-out collapse scenario, the angular momentum profile is shown to flatten out in the inner ∼1000 au (Shu 1977; Yen et al. 2011). Assuming a constant angular momentum profile in the inner envelope down to the disk, an estimation of age can be inferred using the method described by Takahashi et al. (2016). Using Equation (26) in their paper, with specific angular momenta of $(1.2\text{–}3.8) \times 10^{-5}$ km s^{-1} pc, the age of IRAS15398 is expected to be $(0.6\text{–}1.9) \times 10^4$ yr. This is consistent with the age calculated using the mass accretion rate range in Section 5.1.2. These multiple age estimations, small protostellar mass, and seemingly small disk demonstrate that IRAS15398 is likely in its very early stages.

5.3. A Dynamical Overview of the IRAS 15398–3359 Protostellar System

IRAS15398 is a very young, low-mass protostellar system hosting a small protostellar disk and two distinct bipolar outflows. We present a dynamical overview of the IRAS15398 system in Figure 8. We show the episodic outflow ejection lobes (Vazzano et al. 2021), the mean B-field direction (Redaelli et al. 2019), the linear structure interpreted as either a "relic" outflow (Okoda et al. 2021) or perturbed gas due to a nearby possible outflow (Vazzano et al. 2021), and the rotation direction and PA of the disk from our study (Figure 8, left panel). In addition, the previously derived outflow inclination angles (Oya et al. 2014; Yen et al. 2017a) are compared to the

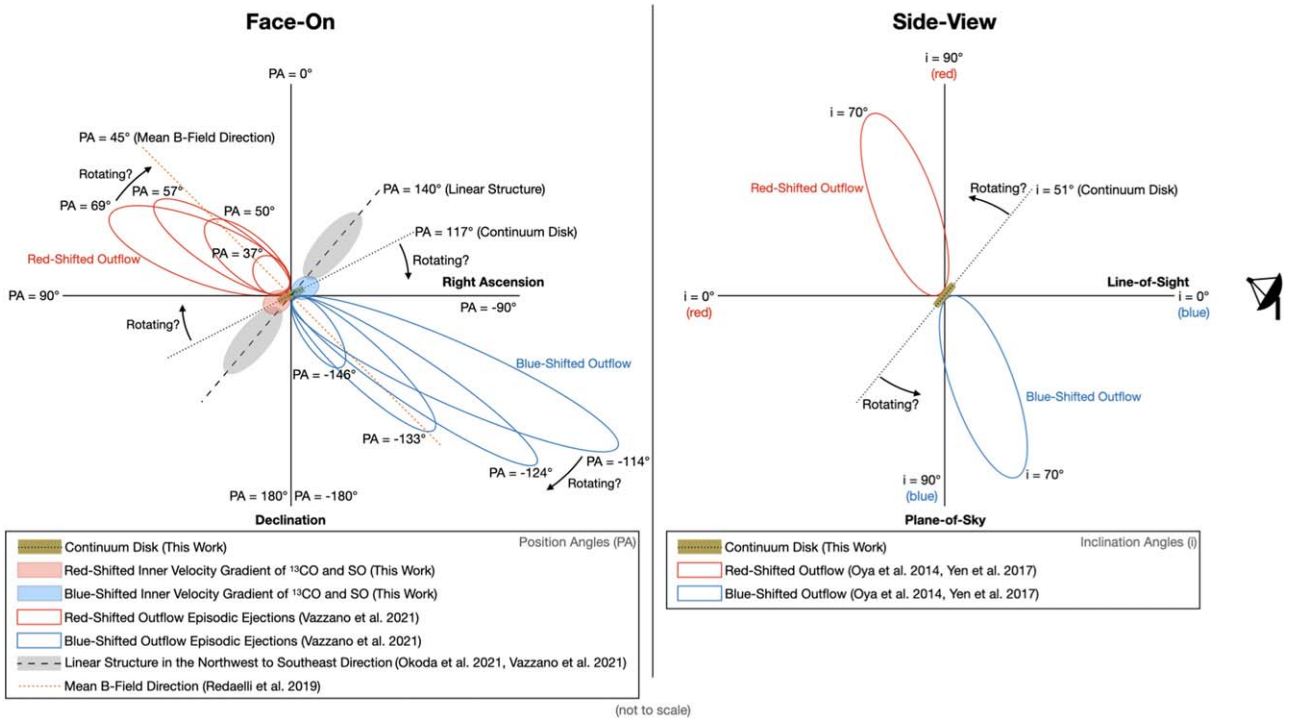

Figure 8. A dynamical schematic of the IRAS15398 protostellar system.

inclination angle found using the geometry of our 2D Gaussian dust continuum fitting (Figure 8, right panel).

Our results show that the PA of the continuum emission is not quite perpendicular to the overall outflow direction found by Vazzano et al. (2021). This could likely be related to the precessing protostellar outflow (Bjerkeli et al. 2016b; Vazzano et al. 2021). The precession is also seen in our ^{12}CO data (Section 3.2.1), where the outflow emission bends in the plane of sky. We quantify this by calculating the difference in the continuum PA between the outflow PAs for the outer and inner episodic ejection lobes found by Vazzano et al. (2021). For the outer red- and blueshifted outflow lobes with PAs of 69° and 246°, the offset from the continuum major axis is ∼48° and ∼51°, respectively. For the inner red- and blueshifted outflow lobes with PAs of 37° and 214°, the offsets are closer to perpendicular at ∼80° and ∼83°, indicating that the central dust emission aligns more perpendicularly with the more recent outflow ejections. One might expect in a perfectly symmetrical collapse that the outflows are perpendicular to the disk major axis. Thus, the offsets indicate that the entire system is precessing. Since no binary is resolved, asymmetric infall seems a more likely scenario for causing the precession. We also note that the mean *B*-field direction is offset by ∼18° from the continuum minor axis. This could help to promote disk formation as found in previous MHD simulations where the angular momentum and *B*-field directional axes are misaligned (e.g., Krumholz et al. 2013; Li et al. 2013; Gray et al. 2018; Tsukamoto et al. 2018; Hirano et al. 2020; Wang et al. 2022). As for the inclination angles, although they seem to be different between the outflows and the disk, understanding the precession of the system in the plane of sky is less robust.

6. Conclusion

We have observed the Class 0 protostar IRAS15398 at high angular resolution with ALMA as part of the eDisk large program. This paper provides an initial analysis to derive various dynamical properties of the protostar-disk system. The main results are as follows:

1. The dust continuum observations show the extended dust structures as found in previous studies but also reveal the small, compact dust disk at a high angular resolution (∼0.″04). The compact dust emission indicates that IRAS15398 is likely a single source but still could be an extremely close binary with a separation of $\lesssim$6 au. From the 2D Gaussian fitting, the 2σ radius of the dust disk is measured to be ∼3.8 au, with a position and inclination angle of 117.°1 and 50.°7, respectively. The disk mass is found to be extremely low, with a value between 0.6M_J and 1.8M_J. Observations at longer wavelengths may be needed to further constrain the disk mass if the dust is optically thick at 1.3 mm. No substructures within the dust disk were found. The molecular lines trace the gas kinematics of the bipolar outflows, inner envelope, and a rotating disk-like structure. The outflow is traced mainly by ^{12}CO and partially by ^{13}CO in the SB+LB observations, while extended emission perpendicular to the outflows is present in the SB-only maps. C^{18}O traces components of the inner envelope, while ^{13}CO and SO show a rotational velocity gradient around the central protostar. The PV diagrams indicate that the velocity structure of SO is likely tracing the rotating disk.
2. We employ SLAM to perform several rotation curve fittings using both single and double power-law profiles. We conclude from the $\tilde{\chi}^2$ values of the single power-law fittings that the ridge traces a Keplerian rotating disk. This results in lower-limit estimates for the protostellar mass and gas disk radius of $0.022 \pm 0.002\,M_\odot$ and 31.2 ± 2.4 au, respectively. The $\tilde{\chi}^2$ for the single power-law edge fittings are less clear, but a conservative upper

limit of the protostellar mass is $\sim 0.1\,M_{\odot}$. Overall, the reduced chi-squared values of the single power-law fits are better than those of the double power-law fits.

3. We estimate the mass accretion rate onto the protostar to be $(1.3\text{–}6.1) \times 10^{-6}\,M_{\odot}\,\mathrm{yr}^{-1}$ and the specific angular momentum at the edge of the protostellar disk to be $(1.2\text{–}3.8) \times 10^{-4}\,\mathrm{km\,s}^{-1}$ pc. The low mass accretion rate implies that there is still a significant amount of mass that can feed the star–disk system. From these two independent measurements, we estimate that the age of the protostar is at least 3600 yr, all the way up to 75,000 yr. At this young age with no clear substructures in the disk, planet formation would likely not yet have started. We estimate a disk-to-stellar mass ratio of <0.06, meaning that the protostar–disk system is gravitationally stable. Additionally, the gas disk measured from our SLAM fitting of SO is >4.2 times larger than the dust disk measured from the dust continuum fitting. This could be either a signpost of dust radial drift or an optical depth effect. Further modeling of the dust continuum and molecular line optical depths could help to confirm which scenario is present in IRAS15398.

Acknowledgments

We thank the anonymous referee for the helpful comments and suggestions on this manuscript. This paper makes use of the following ALMA data: ADS/JAO.ALMA#2019.1.00261.L, ADS/JAO.ALMA#2019.A.00034.S. ALMA is a partnership of ESO (representing its member states), NSF (USA) and NINS (Japan), together with NRC (Canada), NSTC and ASIAA (Taiwan), and KASI (Republic of Korea), in cooperation with the Republic of Chile. The Joint ALMA Observatory is operated by ESO, AUI/NRAO and NAOJ. The National Radio Astronomy Observatory is a facility of the National Science Foundation operated under cooperative agreement by Associated Universities, Inc. This work used high-performance computing facilities operated by the Center for Informatics and Computation in Astronomy (CICA) at National Tsing Hua University. This equipment was funded by the Ministry of Education of Taiwan, the National Science and Technology Council of Taiwan, and National Tsing Hua University. S.-P.L. and T.J.T. acknowledge grants from the National Science and Technology Council (NSTC) of Taiwan 106-2119-M-007-021-MY3, 109-2112-M-007-010-MY3, and 112-2112-M-007-011. N.O. acknowledges support from National Science and Technology Council (NSTC) in Taiwan through the grants NSTC 109-2112-M-001-051, 110-2112-M-001-031, 110-2124-M-001-007, and 111-2124-M-001-005. J.J.T. acknowledges support from NASA XRP 80NSSC22K1159. J.K.J. and R.S. acknowledge support from the Independent Research Fund Denmark (grant No. 0135-00123B). Z.-Y.L. is supported in part by NASA NSSC20K0533 and NSF AST-2307199 and AST-1910106. L.W.L. acknowledges support from NSF AST-2108794. H.-W.Y. acknowledges support from the National Science and Technology Council (NSTC) in Taiwan through the grant NSTC 110-2628-M-001-003-MY3 and from the Academia Sinica Career Development Award (AS-CDA-111-M03). S.T. is supported by JSPS KAKENHI grant Nos. 21H00048 and 21H04495. This work was supported by NAOJ ALMA Scientific Research Grant Code 2022-20A. Z.-Y.D.L. acknowledges support from NASA 80NSSCK1095, the Jefferson Scholars Foundation, the NRAO ALMA Student Observing Support (SOS) SOSPA8-003, the Achievements Rewards for College Scientists (ARCS) Foundation Washington Chapter, the Virginia Space Grant Consortium (VSGC), and UVA research computing (RIVANNA). J.-E.L. is supported by the National Research Foundation of Korea (NRF) grant funded by the Korean government (MSIT) (grant No. 2021R1A2C1011718). C.W.L. is supported by the Basic Science Research Program through the National Research Foundation of Korea (NRF) funded by the Ministry of Education, Science and Technology (NRF- 2019R1A2C1010851), and by the Korea Astronomy and Space Science Institute grant funded by the Korea government (MSIT; Project No. 2022-1-840-05). J.P.W. acknowledges support from NSF AST-2107841. S.N. acknowledges support from the National Science Foundation through the Graduate Research Fellowship Program under grant No. 2236415. Any opinions, findings, and conclusions or recommendations expressed in this material are those of the authors and do not necessarily reflect the views of the National Science Foundation. W.K. was supported by the National Research Foundation of Korea (NRF) grant funded by the Korea government (MSIT) (NRF-2021R1F1A1061794). I.d.G.-M. acknowledges support from grant PID2020-114461GB-I00, funded by MCIN/AEI/10.13039/501100011033. Y.Y. is supported by the International Graduate Program for Excellence in Earth-Space Science (IGPEES), World-leading Innovative Graduate Study (WINGS) Program of the University of Tokyo. Y.A. acknowledges support by NAOJ ALMA Scientific Research Grant code 2019-13B, Grant-in-Aid for Scientific Research (S) 18H05222, and Grant-in-Aid for Transformative Research Areas (A) 20H05844 and 20H05847.

Appendix A
Gallery of Dust Continuum Images

In Figure A1, we present the SB+LB dust continuum maps produced by the eDisk calibration and imaging script for IRAS15398. The properties of each map are shown in Table A1. There is clear extended dust emission in the lower-resolution maps, while increasing the angular resolution shows that the extended emission becomes more resolved out until there is just a compact continuum structure in the highest-resolution maps. The compact structure does appear to be disklike but is somewhat asymmetric. IRAS15398 does not show any signs of binarity up to our highest resolution of 5.8 au.

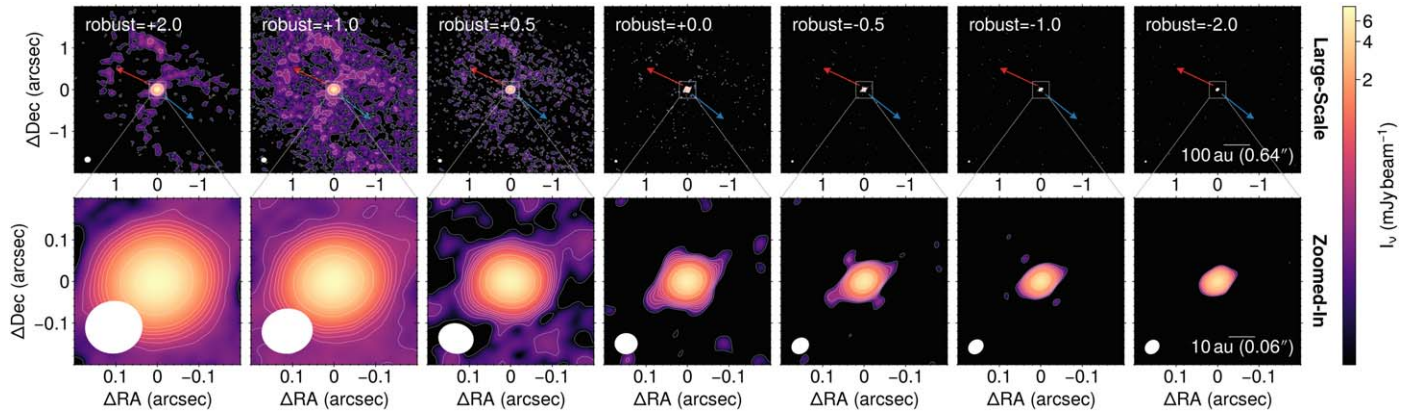

Figure A1. Gallery of SB+LB continuum images from our eDisk observations of IRAS15398 with asinh ($a = 0.001$) scaling. Each robust value made by the imaging script is shown from largest angular resolution (robust = +2.0) on the left to smallest angular resolution (robust = −2.0) on the right. A large-scale view is shown in the top row, while a zoomed-in view is shown in the bottom row. The blue and red arrows represent the overall blue- and redshifted outflow directions found by Vazzano et al. (2021), respectively. The contours in both maps are shown in steps (3, 5, 7, 9, 12, 15, 20, 50, 100)$\sigma_{\rm rms}$, where $\sigma_{\rm rms}$ is the rms noise of each map.

Table A1
Summary of SB+LB Dust Continuum Maps

Robust	Beam Size	Peak Intensity (mJy beam^{-1})	Peak Brightness Temperature (K)	rms Noise (mJy beam^{-1})	S/N
+2.0	$0\farcs137 \times 0\farcs125$ ($-81\fdg8$)	7.79	11.0	0.06	140
+1.0	$0\farcs122 \times 0\farcs107$ ($-82\fdg0$)	7.63	14.2	0.03	237
+0.5	$0\farcs084 \times 0\farcs071$ ($+78\fdg0$)	7.10	28.6	0.02	334
+0.0	$0\farcs054 \times 0\farcs049$ ($-88\fdg0$)	6.47	58.9	0.03	248
−0.5	$0\farcs043 \times 0\farcs036$ ($-55\fdg8$)	5.95	93.4	0.04	157
−1.0	$0\farcs038 \times 0\farcs031$ ($-50\fdg5$)	5.68	114.2	0.06	98
−2.0	$0\farcs037 \times 0\farcs030$ ($-47\fdg4$)	5.61	123.9	0.13	44

Note. Brightness temperatures were computed using the full blackbody equation at a frequency of 225 GHz. The peak intensity and brightness temperature of the continuum maps were found by using a 2″ circular aperture around the center position. The rms noise values of the continuum maps were found by using a 10″ circular aperture in an emission-free area.

Appendix B
Channel Maps of Molecular Lines

In Figures B1–B4, we present the SB+LB molecular line channel maps for IRAS15398. A zoomed-in version of the SO channel map is also provided in Figure B5. Please see Section 3 for more details.

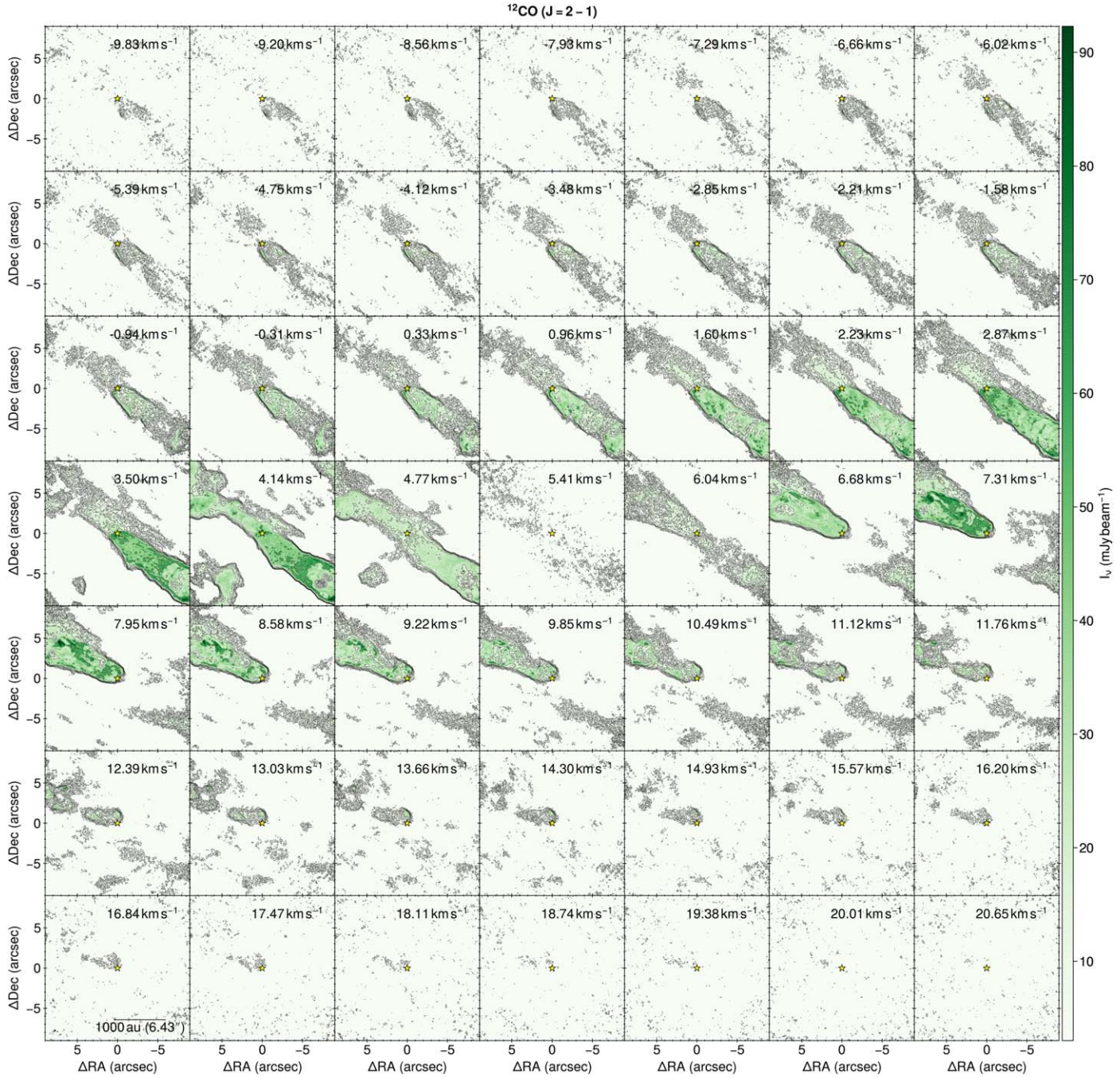

Figure B1. Channel map of the SB+LB ^{12}CO ($J = 2 \rightarrow 1$) molecular line data. The channel velocities are shown in the upper right corner of the panels. The yellow star denotes the central position of IRAS15398 from the 2D Gaussian fitting. The scale bar is shown in the bottom left panel. Contours are shown in steps (3, 5, 7, 9, 12, 15, 20, 50, 100)$\sigma_{\rm rms}$, where $\sigma_{\rm rms}$ is the rms noise of the map. The channel map is centered at 5.41 km s^{-1}, which is the channel closest to the previously derived system velocity of 5.24 km s^{-1} (Yen et al. 2017a).

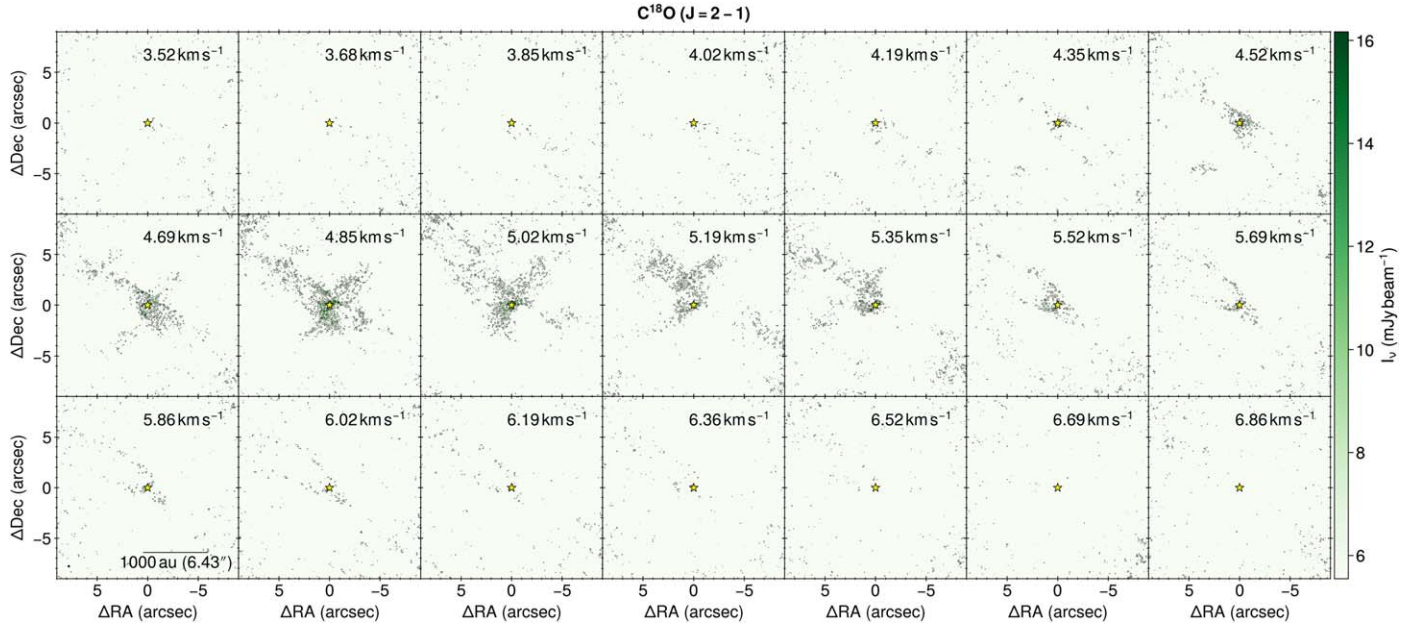

Figure B2. Same as Figure B1, but for $C^{18}O$ ($J = 2 \rightarrow 1$). The channel map is centered at 5.19 km s^{-1}.

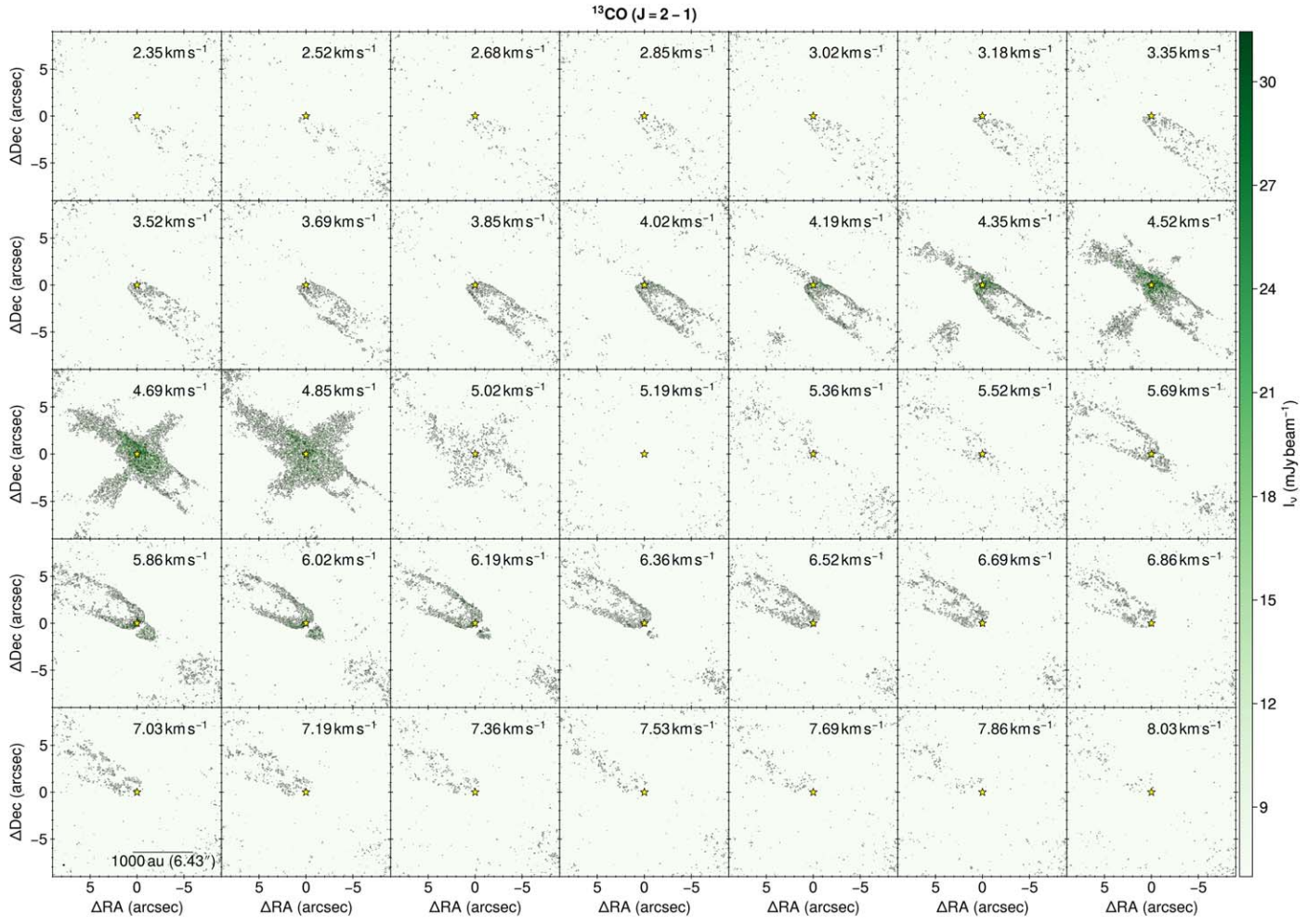

Figure B3. Same as Figure B1, but for ^{13}CO ($J = 2 \rightarrow 1$). The channel map is centered at 5.19 km s^{-1}.

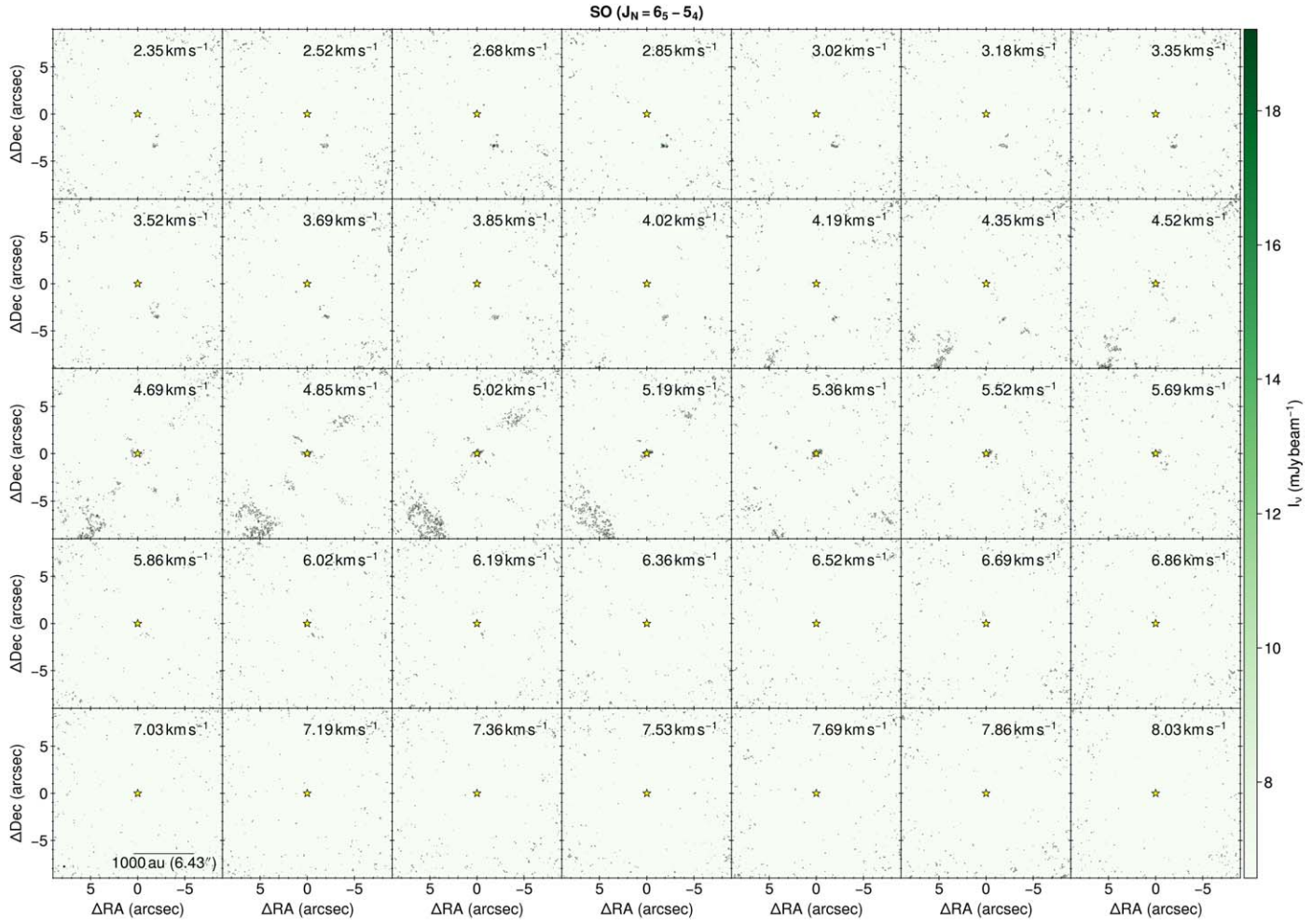

Figure B4. Same as Figure B1, but for SO ($J_N = 6_5 \rightarrow 5_4$). The channel map is centered at 5.19 km s^{-1}.

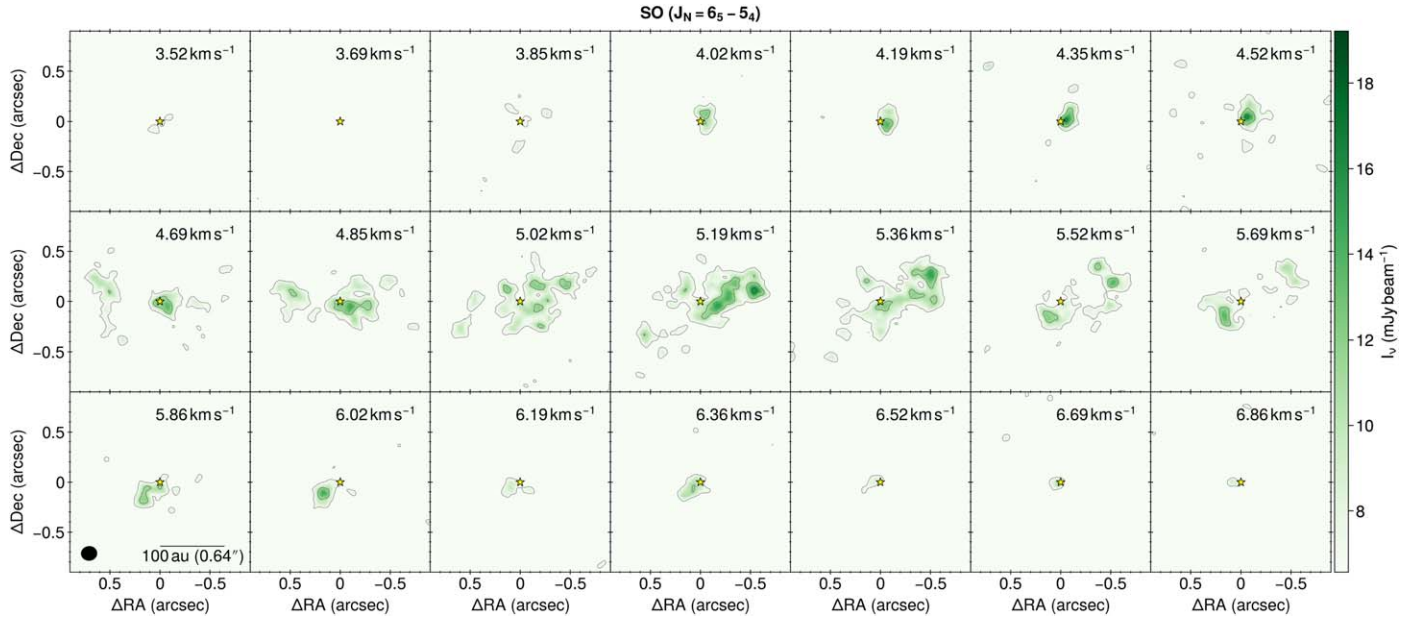

Figure B5. Zoomed-in version of Figure B4 for SO ($J_N = 6_5 \rightarrow 5_4$) showing velocities from 3.52 to 6.86 km s^{-1}. The channel map is centered at 5.19 km s^{-1}.

Appendix C
SB-only Images of Molecular Lines

In Figures C1 and C2, we present the SB-only integrated intensity and intensity-weighted velocity maps for IRAS15398. A summary of the map parameters is shown in Table C1. The estimated rms of the ^{12}CO, C^{18}O, ^{13}CO, and SO integrated intensity maps are 8.79, 1.93, 4.05, and 3.05 mJy beam^{-1} km s^{-1}, respectively. Please see Section 3 for more details.

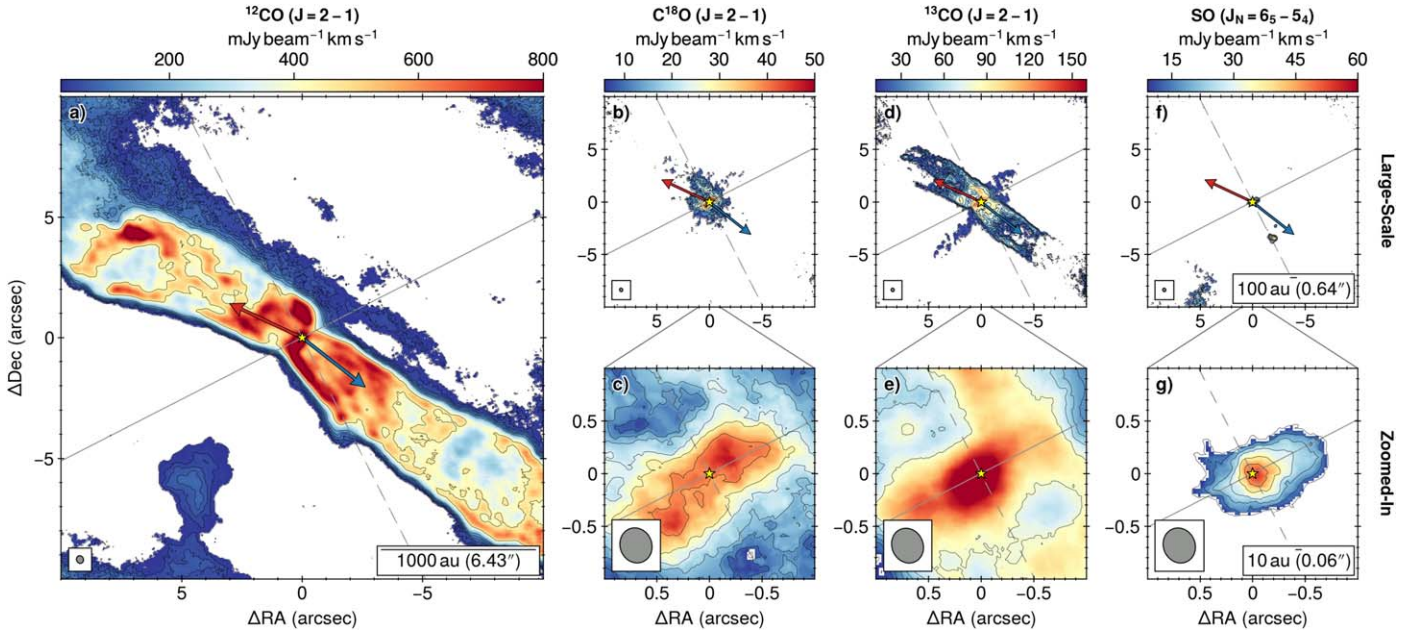

Figure C1. Same as Figure 3, but for the SB-only maps of the representative molecular lines.

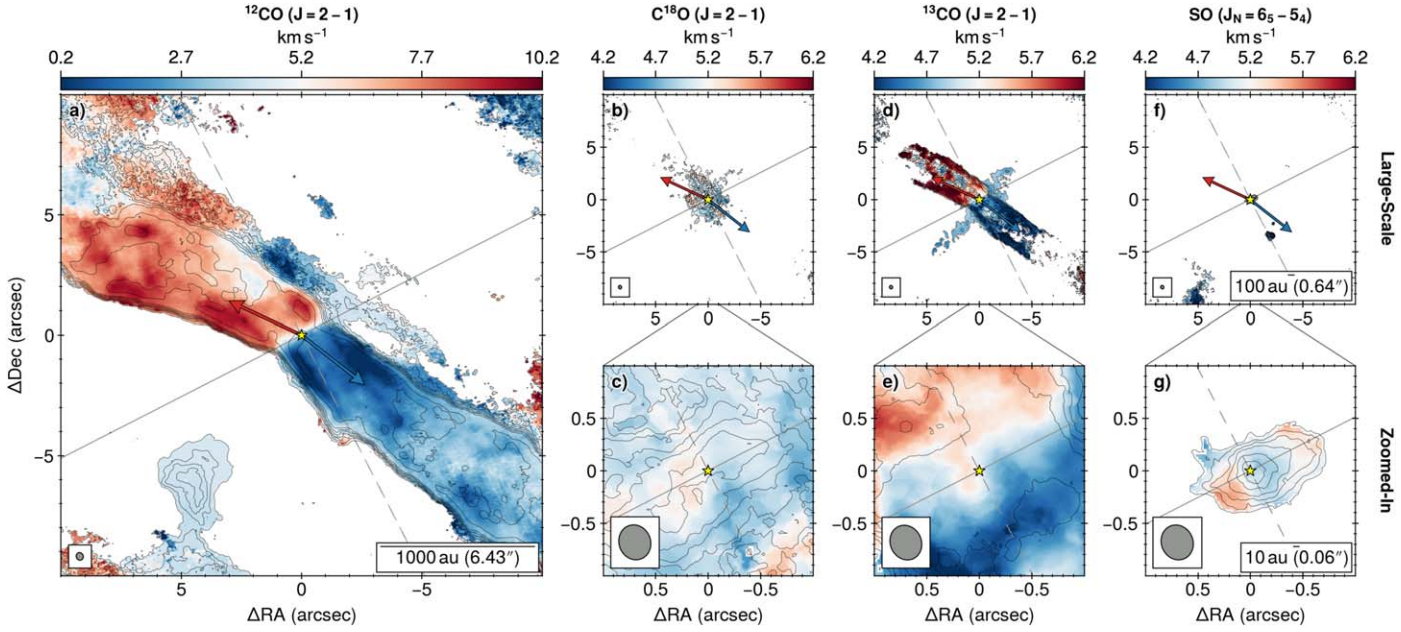

Figure C2. Same as Figure 4, but for the SB-only maps of the representative molecular lines.

Table C1
Summary of Representative SB-only Molecular Line Maps

Molecular Line	Frequency (GHz)	Robust	Beam Size	Velocity Resolution (km s^{-1})	Peak Intensity (mJy beam^{-1})	rms Noise (mJy beam^{-1})
$C^{18}O$ ($J = 2 \rightarrow 1$)	219.56035	+2.0	$0\farcs337 \times 0\farcs301$ ($+20\fdg9$)	0.167	46.2	2.98
SO ($J_N = 6_5 \rightarrow 5_4$)	219.94944	+2.0	$0\farcs338 \times 0\farcs301$ ($+23\fdg8$)	0.167	35.82	3.58
^{13}CO ($J = 2 \rightarrow 1$)	220.39868	+2.0	$0\farcs338 \times 0\farcs295$ ($+25\fdg3$)	0.167	105.5	4.09
^{12}CO ($J = 2 \rightarrow 1$)	230.53800	+2.0	$0\farcs324 \times 0\farcs288$ ($+22\fdg1$)	0.635	216.6	1.98

Note. The values listed here were obtained from the maps using SB-only observations. The peak intensities of the line maps were found by using a 2″ circular aperture around the center position on the channel with the highest intensity. The rms noise values of the line maps were found by using a 10″ circular aperture in an emission-free area around the center position on a line-free channel near the beginning of the datacube.

ORCID iDs

Travis J. Thieme https://orcid.org/0000-0003-0334-1583
Shih-Ping Lai https://orcid.org/0000-0001-5522-486X
Nagayoshi Ohashi https://orcid.org/0000-0003-0998-5064
John J. Tobin https://orcid.org/0000-0002-6195-0152
Jes K. Jørgensen https://orcid.org/0000-0001-9133-8047
Jinshi Sai (Insa Choi) https://orcid.org/0000-0003-4361-5577
Yusuke Aso https://orcid.org/0000-0002-8238-7709
Jonathan P. Williams https://orcid.org/0000-0001-5058-695X
Yoshihide Yamato https://orcid.org/0000-0003-4099-6941
Yuri Aikawa https://orcid.org/0000-0003-3283-6884
Itziar de Gregorio-Monsalvo https://orcid.org/0000-0003-4518-407X
Ilseung Han https://orcid.org/0000-0002-9143-1433
Woojin Kwon https://orcid.org/0000-0003-4022-4132
Chang Won Lee https://orcid.org/0000-0002-3179-6334
Jeong-Eun Lee https://orcid.org/0000-0003-3119-2087
Zhi-Yun Li https://orcid.org/0000-0002-7402-6487
Zhe-Yu Daniel Lin https://orcid.org/0000-0001-7233-4171
Leslie W. Looney https://orcid.org/0000-0002-4540-6587
Suchitra Narayanan https://orcid.org/0000-0002-0244-6650
Nguyen Thi Phuong https://orcid.org/0000-0002-4372-5509
Adele L. Plunkett https://orcid.org/0000-0002-9912-5705
Alejandro Santamaría-Miranda https://orcid.org/0000-0001-6267-2820
Rajeeb Sharma https://orcid.org/0000-0002-0549-544X
Shigehisa Takakuwa https://orcid.org/0000-0003-0845-128X
Hsi-Wei Yen https://orcid.org/0000-0003-1412-893X

References

Allen, A., Li, Z.-Y., & Shu, F. H. 2003, ApJ, 599, 363
ALMA Partnership, Brogan, C. L., Pérez, L. M., et al. 2015, ApJL, 808, L3
Andrews, S. M., Huang, J., Pérez, L. M., et al. 2018, ApJL, 869, L41
Andrews, S. M., Wilner, D. J., Hughes, A. M., et al. 2012, ApJ, 744, 162
Ansdell, M., Williams, J. P., Trapman, L., et al. 2018, ApJ, 859, 21
Ansdell, M., Williams, J. P., van der Marel, N., et al. 2016, ApJ, 828, 46
Aso, Y., & Machida, M. N. 2020, ApJ, 905, 174
Aso, Y., Ohashi, N., Aikawa, Y., et al. 2017, ApJ, 849, 56
Aso, Y., Ohashi, N., Saigo, K., et al. 2015, ApJ, 812, 27
Aso, Y., & Sai, J. 2023, jinshisai/SLAM: First Release of SLAM, v1.0.0, Zenodo, doi:10.5281/zenodo.7783868
Bae, J., Isella, A., Zhu, Z., et al. 2022, arXiv:2210.13314
Beckwith, S. V. W., Sargent, A. I., Chini, R. S., & Guesten, R. 1990, AJ, 99, 924
Bjerkeli, P., Jørgensen, J. K., Bergin, E. A., et al. 2016a, A&A, 595, A39
Bjerkeli, P., Jørgensen, J. K., & Brinch, C. 2016b, A&A, 587, A145
Boyden, R. D., & Eisner, J. A. 2020, ApJ, 894, 74
Burrows, A., Marley, M., Hubbard, W. B., et al. 1997, ApJ, 491, 856
CASA Team, Bean, B., Bhatnagar, S., et al. 2022, PASP, 134, 114501
de Gregorio-Monsalvo, I., Ménard, F., Dent, W., et al. 2013, A&A, 557, A133
Dzib, S. A., Loinard, L., Ortiz-León, G. N., Rodríguez, L. F., & Galli, P. A. B. 2018, ApJ, 867, 151
Enoch, M. L., Evans, N. J. I., Sargent, A. I., et al. 2008, ApJ, 684, 1240
Facchini, S., Birnstiel, T., Bruderer, S., & van Dishoeck, E. F. 2017, A&A, 605, A16
Galli, P. A. B., Bouy, H., Olivares, J., et al. 2020, A&A, 643, A148
Gray, W. J., McKee, C. F., & Klein, R. I. 2018, MNRAS, 473, 2124
Guilloteau, S., Simon, M., Piétu, V., et al. 2014, A&A, 567, A117
Harsono, D., Bjerkeli, P., van der Wiel, M. H. D., et al. 2018, NatAs, 2, 646
Harsono, D., van Dishoeck, E. F., Bruderer, S., Li, Z. Y., & Jørgensen, J. K. 2015, A&A, 577, A22
Hartmann, L., Cassen, P., & Kenyon, S. J. 1997, ApJ, 475, 770
Hayashi, C., & Nakano, T. 1963, PThPh, 30, 460
Hennebelle, P., & Ciardi, A. 2009, A&A, 506, L29
Hennebelle, P., & Fromang, S. 2008, A&A, 477, 9
Hirano, S., Tsukamoto, Y., Basu, S., & Machida, M. N. 2020, ApJ, 898, 118
Joos, M., Hennebelle, P., & Ciardi, A. 2012, A&A, 543, A128
Jørgensen, J. K., van Dishoeck, E. F., Visser, R., et al. 2009, A&A, 507, 861
Jørgensen, J. K., Visser, R., Sakai, N., et al. 2013, ApJL, 779, L22
Kristensen, L. E., van Dishoeck, E. F., Bergin, E. A., et al. 2012, A&A, 542, A8
Krumholz, M. R., Crutcher, R. M., & Hull, C. L. H. 2013, ApJL, 767, L11
Kumar, S. S. 1963a, ApJ, 137, 1121
Kumar, S. S. 1963b, ApJ, 137, 1126
Lee, C.-F. 2020, A&ARv, 28, 1
Li, Z.-Y., Krasnopolsky, R., & Shang, H. 2013, ApJ, 774, 82
Lodato, G., & Rice, W. K. M. 2004, MNRAS, 351, 630
Lodato, G., & Rice, W. K. M. 2005, MNRAS, 358, 1489
Machida, M. N., & Matsumoto, T. 2012, MNRAS, 421, 588
Manara, C. F., Ansdell, M., Rosotti, G. P., et al. 2023, in ASP Conf. Ser. 534, Protostars and Planets VII, ed. S.-i. Inutsuka (San Francisco, CA: ASP), 539
Maret, S., Maury, A. J., Belloche, A., et al. 2020, A&A, 635, A15
McMullin, J. P., Waters, B., Schiebel, D., Young, W., & Golap, K. 2007, in ASP Conf. Ser. 376, Astronomical Data Analysis Software and Systems XVI, ed. R. A. Shaw, F. Hill, & D. J. Bell (San Francisco, CA: ASP), 127
Mellon, R. R., & Li, Z.-Y. 2008, ApJ, 681, 1356
Murillo, N. M., Lai, S.-P., Bruderer, S., Harsono, D., & van Dishoeck, E. F. 2013, A&A, 560, A103
Öberg, K. I., Guzmán, V. V., Walsh, C., et al. 2021, ApJS, 257, 1
Offner, S. S. R., & Chaban, J. 2017, ApJ, 847, 104
Ohashi, N., Hayashi, M., Ho, P. T. P., & Momose, M. 1997, ApJ, 475, 211
Ohashi, N., Saigo, K., Aso, Y., et al. 2014, ApJ, 796, 131
Ohashi, N., Tobin, J. J., Jørgensen, J. K., et al. 2023, ApJ, 951, 8
Okoda, Y., Oya, Y., Francis, L., et al. 2021, ApJ, 910, 11
Okoda, Y., Oya, Y., Francis, L., et al. 2023, ApJ, 948, 127
Okoda, Y., Oya, Y., Sakai, N., et al. 2018, ApJL, 864, L25
Oya, Y., Sakai, N., Sakai, T., et al. 2014, ApJ, 795, 152
Panić, O., Hogerheijde, M. R., Wilner, D., & Qi, C. 2009, A&A, 501, 269
Redaelli, E., Alves, F. O., Santos, F. P., & Caselli, P. 2019, A&A, 631, A154
Sai, J., Ohashi, N., Saigo, K., et al. 2020, ApJ, 893, 51
Sakai, N., Oya, Y., Higuchi, A. E., et al. 2017, MNRAS, 467, L76
Sakai, N., Sakai, T., Hirota, T., et al. 2014, Natur, 507, 78
Santamaría-Miranda, A., de Gregorio-Monsalvo, I., Plunkett, A. L., et al. 2021, A&A, 646, A10
Segura-Cox, D. M., Looney, L. W., Tobin, J. J., et al. 2018, ApJ, 866, 161
Segura-Cox, D. M., Schmiedeke, A., Pineda, J. E., et al. 2020, Natur, 586, 228

Sheehan, P. D., & Eisner, J. A. 2018, ApJ, 857, 18
Sheehan, P. D., Tobin, J. J., Federman, S., Megeath, S. T., & Looney, L. W. 2020, ApJ, 902, 141
Sheehan, P. D., Tobin, J. J., Looney, L. W., & Megeath, S. T. 2022, ApJ, 929, 76
Sheehan, P. D., Wu, Y.-L., Eisner, J. A., & Tobin, J. J. 2019, ApJ, 874, 136
Shu, F. H. 1977, ApJ, 214, 488
Simon, M., Dutrey, A., & Guilloteau, S. 2000, ApJ, 545, 1034
Stahler, S. W., Shu, F. H., & Taam, R. E. 1980, ApJ, 241, 637
Tabone, B., Cabrit, S., Bianchi, E., et al. 2017, A&A, 607, L6
Takahashi, S. Z., Tomida, K., Machida, M. N., & Inutsuka, S.-i. 2016, MNRAS, 463, 1390
Teague, R. 2019, RNAAS, 3, 74
Teague, R., & Foreman-Mackey, D. 2018, RNAAS, 2, 173
Tobin, J. J., Hartmann, L., Chiang, H.-F., et al. 2012, Natur, 492, 83
Tobin, J. J., Looney, L. W., Wilner, D. J., et al. 2015, ApJ, 805, 125
Tobin, J. J., Sheehan, P. D., Megeath, S. T., et al. 2020, ApJ, 890, 130
Trapman, L., Ansdell, M., Hogerheijde, M. R., et al. 2020, A&A, 638, A38
Tsukamoto, Y., Okuzumi, S., Iwasaki, K., Machida, M. N., & Inutsuka, S. 2018, ApJ, 868, 22
Tychoniec, Ł., Manara, C. F., Rosotti, G. P., et al. 2020, A&A, 640, A19
van Gelder, M. L., Tabone, B., van Dishoeck, E. F., & Godard, B. 2021, A&A, 653, A159
Vazzano, M. M., Fernández-López, M., Plunkett, A., et al. 2021, A&A, 648, A41
Wang, W., Väisälä, M. S., Shang, H., et al. 2022, ApJ, 928, 85
Yamato, Y., Aikawa, Y., Ohashi, N., et al. 2023, ApJ, 951, 11
Yen, H.-W., Gu, P.-G., Hirano, N., et al. 2019, ApJ, 880, 69
Yen, H.-W., Koch, P. M., Takakuwa, S., et al. 2015a, ApJ, 799, 193
Yen, H.-W., Koch, P. M., Takakuwa, S., et al. 2017a, ApJ, 834, 178
Yen, H.-W., Takakuwa, S., Chu, Y.-H., et al. 2017b, A&A, 608, A134
Yen, H.-W., Takakuwa, S., Koch, P. M., et al. 2015b, ApJ, 812, 129
Yen, H.-W., Takakuwa, S., & Ohashi, N. 2011, ApJ, 742, 57
Yen, H.-W., Takakuwa, S., Ohashi, N., et al. 2014, ApJ, 793, 1
Zucker, C., Speagle, J. S., Schlafly, E. F., et al. 2020, A&A, 633, A51